VOLUME 18, NOMOR 3 (2022)
ISSN, p: 1858-036X
e: 2460-4682

JFA

Jurnal Fisika dan Aplikasinya

DAFTAR ISI

DEPARTEMEN FISIKA, FAKULTAS SAINS DAN ANALITIKA DATA
Institut Teknologi Sepuluh Nopember (ITS) Surabaya

JFA (Jurnal Fisika dan Aplikasinya)

Preface

In the October 2022 issue of Volume 18 Number 3, JFA (Jurnal Fisika dan Aplikasinya) presents five (5) scientific articles related to the fields of Instrumentation Physics, Astrophysics, Geophysics, and Theoretical Physics. The editor in chief expressed his gratitude to Endarko, Ph.D.; Triswantoro Putro, M.Si.; Heru Sukamto, M.Si.; Dr.rer.nat Bintoro Anang Subagyo; Dr. M. Arif Bustomi; Dr. Lila Yuwana; Dr. Suyatno; Dr. Ali Yunus Rohedi; and Dr. Eny Latifah, who has helped the JFA editorial for the review the manuscripts in this issue, and do not forget to thank the authors of the scientific articles who have trusted JFA as a medium to communicate the results of research and scientific studies so that they can be disseminated to physics observer.

On this occasion, the editorial team invited and gave the opportunity to researchers in related fields to publish their research results through this journal. Hopefully the articles in this journal are useful for readers and the development of physics and its applications.

Editor

Journal Contact:
Departemen Fisika, Fakultas Sains dan Analitika Data, Kampus ITS Keputih Sukolilo, Surabaya 60111
Telp./Fax.: +62 315943351;
E-mail: jfa.fisika.its@gmail.com; jfa@physics.its.ac.id
website: http://IPTEK.its.ac.id/index.php/jfa

Development of Chobmons Prototype: Cholesterol and Blood Sugar Level Monitoring System Based on Internet of Things (IoT) using Blynk Application

Heni Sumarti*,[1] Tria Nurmar'atin,[1] Hamdan Hadi Kusuma,[1] Istikomah,[1] and Irman Said Prastyo[1]

[1]*Department of Physics, Faculty of Science and Technology, Universitas Islam Negeri Walisongo Semarang, Jl. Prof. Dr. Hamka Km. 1, Semarang, Jawa Tengah 50185, Indonesia*

Abstract: In the era of the industrial revolution 4.0, we need remote technology and products that d not created new medical waste piles. An unhealthy lifestyle can cause many diseases, either degenerative diseases, namely over rate cholesterol and blood sugar level. High cholesterol and blood sugar levels are causes of major influence on atherosclerosis, stroke, micro-vascular, and cardiovascular complications. We offer a non-invasive cholesterol and blood sugar monitoring device based on red LED and infrared light absorption using the Nellcor DS-100A sensor. This technology can help reduce cumulative medical waste and help health workers to monitor patients remotely. This study used ten random samples to calibrate cholesterol and blood sugar levels. The coefficient of determination values were 0.9580 and 0.9581, respectively, which gave excellent values so that the study is continued by collecting data. Data retrieval use 20 random sample data to measure cholesterol and blood sugar levels, the average accuracy prototype is 90.26% and 91.16%, respectively. It shows great potential in determining estimation value at cholesterol and blood sugar levels. The monitoring system can show the data on the LCD display in Blynk Application with the average time required of 1.07 s.

Keywords: Nellcor DS-100A; Cholesterol and Blood Sugar; Monitoring system

*Corresponding author: heni_sumarti@walisongo.ac.id

Article history: Received 14 Maret 2022, Accepted 28 September 2022, Published October 2022.
http://dx.doi.org/10.12962/j24604682.v18i3.12532

I. INTRODUCTION

In the era of Industrial Revolution 4.0 and COVID-19 pandemics, we need remote technology and products that have not created new medical waste piles. An unhealthy lifestyle during work from home in COVID-19 pandemics, which is not balanced with exercise and healthy food, can cause many diseases [1–4], including degenerative diseases, namely over rate cholesterol and blood sugar level. High cholesterol and blood sugar levels are causes of major influence on atherosclerosis, stroke, micro-vascular and cardiovascular complications [5, 6]. Preventive measures are needed to regularly check cholesterol and blood sugar levels monitored by health workers, thus their levels can be controlled. Measuring and monitoring tools for cholesterol and blood sugar levels are currently only available in certain health institutions [7]. It generally uses an invasive method and cannot be monitored directly by health workers [6]. Therefore, it is necessary to have a new alternative to make it easier for a health worker to check patients' cholesterol and blood sugar levels remotely.

Changes in blood flow can be detected by providing light from an LED and then measuring the amount of light received by the photodiode [8]. An oximeter sensor can measure oxygen saturation in the blood by using light at a certain wavelength through the tissue (usually the index finger) [8]. Cholesterol deposits associated with atherosclerosis are thought to increase with age [10]; it blocks the blood vessels in the form of plaque [10, 11] . Meanwhile, blood sugar levels cause an increase in blood concentration [12]. There is an opportunity to measure cholesterol and blood sugar levels using an oximeter and the Nellcor DS-100A sensors.

In the previous study, the monitoring system measured the glucose level in the blood using an oximeter sensor resulting in an accuracy of up to 97% [13]. Research by Nurmar'atin et. al. [14] developed a telemedicine system to measure cholesterol levels in the blood delivers an accuracy of 82.76% using the oximeter DS-100A. These results indicate that the oximeter sensor can be developed to measure blood sugar and cholesterol levels non-invasively which can be used for estimation. Therefore, in this research, a monitoring system was developed to estimate blood sugar and cholesterol levels in real-time. This study aims to develop Chobmons prototype and is expected to be used as a reference instrument for health workers to monitor cholesterol and blood sugar levels remotely.

II. METHOD

The research samples were people with normal or high cholesterol and blood sugar levels in the age range of 20-60 years, both male and female. The number of samples was ten random samples for prototype calibration, while the number of samples for the accuracy test of the prototype system was

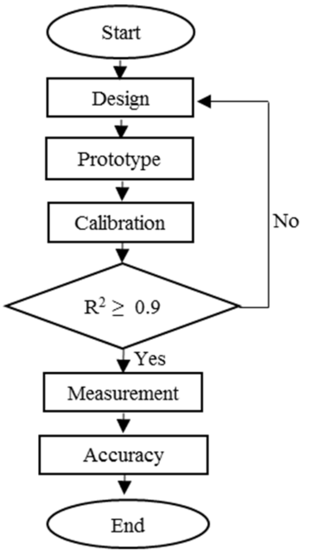

FIG. 1: Schematic of the research procedure.

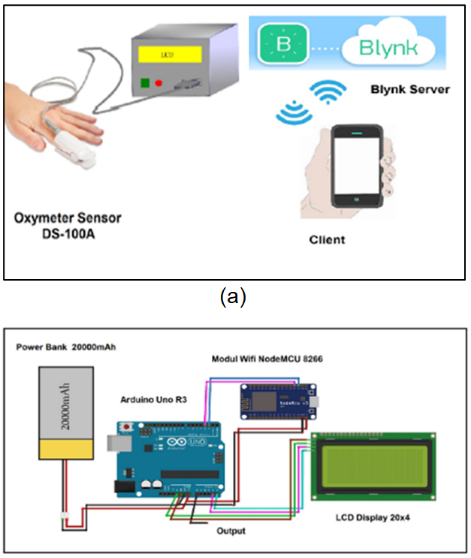

(a)

(b)

FIG. 2: The Chobmons prototype design: (a) monitoring system and (b) hardware components.

20 random samples. The standard measurement instrument used is Autocheck 3-in-1 to measure cholesterol and blood sugar levels. It has received a distribution permit from the Indonesian Ministry of Health with AKL 20101311321. The sample measured using a standard instrument is a fingertip capillary blood, while prototypes hold fingertips in a Nellcor DS-100A sensor for 5 seconds. The measurement using the prototype system is five times to test the stability of the prototype, then the results is averaged to process the data. Data collection was carried out by measuring blood sugar and cholesterol levels using the Chobmons prototype, followed by taking blood using standard tools.

The schematic of the research procedure is shown in Fig. 1. The first stage is the design of the Chobmons prototype so that the prototype can work properly. The second stage is the manufacture of the prototype instrument, followed by calibration and measurement. Measurement aims to get the accuracy of the prototype system. The last step is to develop the monitoring system by synchronizing the Arduino IDE software and the Blynk application so that the data that appears on the LCD screen of the device can be displayed in the Blynk application.

The Chobmons prototype design is shown in Fig. 2. The object of measurement is the tip of the index finger of the sample to detect cholesterol and blood sugar levels by utilizing absorption from red and infrared light. When the tool is turned on, the power bank provides voltage and runs the transmitter circuit. Analog data is processed by Arduino Uno R3 to be displayed on a 20x4 LCD screen in digital form. Then the data is sent by the Node MCU module to the Blynk Application and can be accessed directly via Android.

Calibration is carried out to obtain a linear tradeline using ten random samples. The linear tradeline is obtained by comparing the ADC (Analog to Digital Converter) value of the prototype system and cholesterol and blood sugar levels on a standard measuring instrument (Autocheck 3-in-1). The degree of relationship value assessment will be served using a simple linear regression formula, $y = a + bx$, where y is the result value of standard measuring instruments, a and b are constant, and x is the ADC value of the prototype system measurement. The linear tradeline obtained is used as a conversion factor for the ACD value (mV) into cholesterol and blood sugar levels (mg/dl), while the coefficient of determination R^2 is used to measure the prototype's success in data converting.

The accuracy system test compares the Chobmons prototype and standard measuring instruments in the mg/dl unit. Sampling was done by measuring cholesterol and blood sugar levels in 20 random samples, respectively. Sampling was carried out in two ways: (1) taking a blood sample at the tip of the finger artery using a standard invasive measuring instrument (Autocheck 3-in-1); and (2) attaching the finger to the Nellcor DS-100A sensor on a non-invasive measuring instrument to measure cholesterol and blood sugar levels within 5 seconds. The accuracy of the prototype can be calculated using Eq. (1).

$$Accuracy = 100\% - \frac{Standard - measurement - prototype}{Standard - measurement} \times 100\% \quad (1)$$

The manufacture of the monitoring system in this study was designed using Arduino IDE 1.8.13 software and Blynk Apps. This software is used to program a microcontroller used in non-invasive measurement devices using the Internet of Things (IoT). The data is connected to the server to be displayed in the Blynk application. The function test of the monitoring system is carried out by looking at the data display on the Blynk application. The system can function properly if the data displayed on the LCD screen can appear in the Blynk application display with the same value. Data retrieval was carried out ten times to test the display and speed of data transfer displayed in the Blynk application.

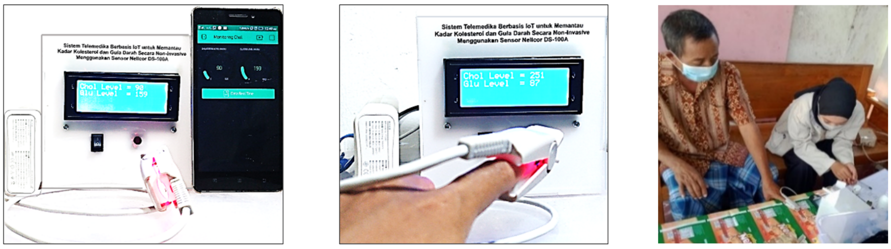

(a) (b) (c)

FIG. 3: (a) The Chobmons prototype instrument, (b) measurements of cholesterol and blood sugar levels using the Nellcor DS-100A sensor via fingertip, and (c)an illustration of data collecting process.

III. RESULTS AND DISCUSSION

A. Results

The prepared Chobmons prototype for measuring cholesterol and blood sugar levels using the Nellcor DS-100A sensor is shown in Fig. 3. The Chobmons prototype consists of a Nellcor DS-100A sensor, 20x4 LCD, an on/off button, a reset button, a power bank, and a microcontroller unit. The Nellcor DS-100A sensor is used as a finger scanner to detect cholesterol and blood sugar levels by utilizing red and infrared light at certain wavelengths. The 20x4 LCD screen displays the values of cholesterol and blood sugar levels. The on/off button turns the appliance on and off. The reset button is used to set the device back to its initial state. The power bank is used as a voltage source to power the device. The microcontroller unit is the main part that runs the tool, or it can be said the brain of the tool.

The calibration result by taking ten random samples data is plotted in a graph using the Microsoft Excel program, then a linear tradeline and the coefficient of determination are generated. Fig. 4(a) shows the relationship between the average ADC value of red LED and cholesterol levels in 10 random samples. The linear tradeline obtained is $y = 0.124x + 90.376$, while the coefficient determination is 0.958. The linear relationship between ADC of red LED and cholesterol levels in the blood is directly proportional, so the higher the cholesterol levels in the blood, the higher the ADC value of red LED. Fig. 4(b) presents the relationship between the average ADC value of infrared light and blood sugar levels in 10 random samples. The linear tradeline obtained is $y = -0.114x + 159.04$, while the coefficient determination is 0.9581. The linear relationship between ADC of infrared light and blood sugar levels is inversely proportional, so the higher the blood sugar level in the blood, the lower ADC value of infrared light value, and vice versa. This linear tradeline equation is the formula for converting the ADC value into the cholesterol and blood sugar level. Based on the coefficient determination, the linear relationship between the ADC value of the prototype instrument and cholesterol and blood sugar levels value of the standard instrument is compelling [15], so the testing of the prototype instrument can continue at the next stage.

The result of measurement on 20 random samples is shown in Table I. The measurement results of maximum cholesterol and blood sugar levels can be achieved if the subject does not perform strenuous physical activity at least 15 minutes before the measurement begins [16], so that during the measurement process, the subject is ensured to be at rest. The measurement of cholesterol and sugar levels using the prototype instrument is the average value of five data. The average accuracy in cholesterol level measurement is 90.26%, while the average accuracy in sugar level measurement is 91.16%.

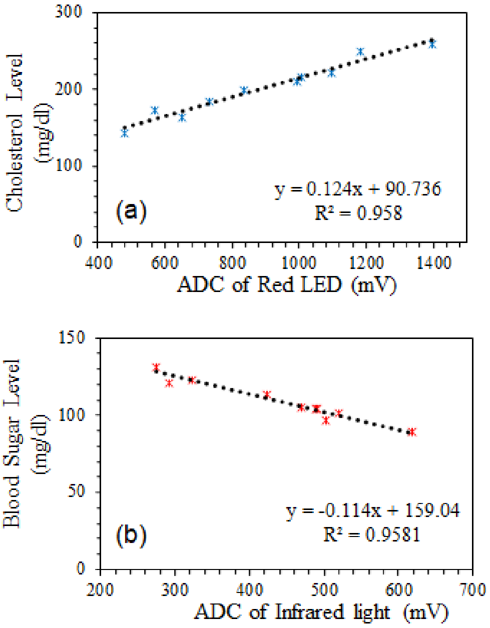

FIG. 4: The graph of calibration in measurement at (a) cholesterol level and (b) blood sugar level.

Furthermore, the experiment was carried out by measuring the data transfer time from the LCD display to the Blynk application. Table II shows the screen display test of the blynk application and also the data transfer speed. The seven data that appeared on the LCD screen managed to appear on the Blynk application screen with an average speed of 1.07 s. The results show that all the data that appears on the LCD screen of the prototype tool can be displayed in the Blynk application.

TABLE I: The Accuracy of the designed Chobmons prototype.

No	Cholesterol level		Accuracy (%)	Blood Sugar level		Accuracy (%)
	Autocheck 3-in-1 (mg/dl)	Prototype (mg/dl)		Autocheck 3-in-1 (mg/dl)	Prototype (mg/dl)	
1	241	196.01	81.33	69	68.39	99.10
2	225	261.09	83.96	98	120.60	81.26
3	198	194.55	98.26	104	109.95	94.59
4	183	204.05	88.50	123	122.15	99.30
5	167	128.13	76.73	109	136.42	79.90
6	143	150.38	94.84	107	122.15	87.60
7	210	180.26	85.84	106	125.07	84.75
8	173	161.39	93.29	121	125.71	96.26
9	184	181.53	98.66	124	111.66	88.95
10	163	171.48	94.79	106	122.67	86.41
11	215	215.55	99.74	95	129.86	73.16
12	147	165.71	87.27	131	127.80	97.50
13	184	220.54	80.14	119	129.38	91.98
14	154	176.54	85.36	105	105.48	99.54
15	237	194.47	82.06	101	104.43	96.71
16	194	165.93	85.53	89	88.43	99.35
17	222	226.99	97.75	91	74.20	77.36
18	258	264.06	97.65	117	126.60	92.42
19	250	237.16	94.86	104	103.13	99.16
20	211	214.04	98.56	113	110.73	97.95

TABLE II: Monitoring system test.

No	Display on LCD	Display on Blynk	Average data transfer (s)
1	Cholesterol	Succeed	1.4
2	Blood Sugar	Succeed	1.1
	Average		1.07

B. Discussions

The ADC value in cholesterol level measurement is using LED red based on the cholesterol maximum absorbance-value in the wavelength range of 550-750 nm [17–19]. Meanwhile, blood sugar level measurement is using ADC value at near-infrared. This is based on measuring blood sugar levels which is effective using near-infrared at wavelengths between 850-1650 nm [18–21]. The Nellcor DS-100A sensor emits the red and infrared light alternately, then captured by a photodiode. Several body parts absorb the light from the red and infrared LEDs at the measurement location (fingertip), referred to as light absorbers. These components are skin, tissue, venous blood, and arterial blood. If the light absorption in the valley (which includes all light absorbers) is subtracted from the light absorption at the peak, then, in theory, the resulting value represents the blood absorption characteristic and is considered as arterial blood flow [8].

The relationship between ADC in red light and cholesterol levels is directly proportional; the higher the cholesterol level, the less red light is absorbed, and the photodiode captures the more light after passing through the finger. In reverse, the lower the cholesterol level in the blood, the lower the red light that passes through the finger and is detected by the photodiode. The type of cholesterol in the blood that flows the most in the arteries is LDL (Low-Density Lipoprotein) cholesterol, which is about 66% of the total cholesterol in the blood [24]; it is also known as bad cholesterol with a low density. LDL cholesterol is the cause of several heart diseases [24], so this is the most important part that must be monitored to always be in normal condition. LDL cholesterol is a plaque that sticks to the arteries of the blood [25], so it does not increase blood concentration. This condition follows Beer Lambert's law; the absorbance value of light absorbed by the material in a particular solution will be equal to the concentration of the solution [26].

The ADC value in infrared light is inversely proportional to blood sugar levels; the higher the blood sugar level, the higher the infrared light is absorbed so that only a small amount passes through the finger and is detected by the photodiode. Otherwise, the lower the blood sugar level, the higher the infrared light that the photodiode can detect after passing through the finger. Blood sugar refers to the level of sugar in the blood formed by carbohydrates in the food and drinks we consume, excess blood sugar in the body causes diabetes mellitus [27], increasing blood concentration. This condition follows Beer Lambert's law; the magnitude of the absorption value will be proportional to the concentration of the test substance [26].

The average of accuracy Chobmons prototype to measuring cholesterol and blood sugar levels is 90.26% and 91.16%, respectively. It is indicating that the prototype of this instrument cannot be used as a standard measuring instrument on medical instruments yet, which is must be more than 95% [28, 29]. The results of this study show an increase in the accuracy compared to previous studies on measuring cholesterol levels by 7.5% [14]. While the highest level of accuracy in blood sugar is 99.54% with an increase of 2.54% [30]. This condition is because the light on the skin layer can interfere, affecting the sensor's intensity; correction is an important way to get good measurement results [13]. Nevertheless, it shows great potential in determining estimation value at cholesterol and blood sugar levels. We can improve accuracy by providing corrections to the algorithm and or circuit on the prototype. The monitoring system can work well by displaying real-time data monitored using Android on the Blynk application. This condition can make it easier for health workers to remotely monitor high cholesterol and blood sugar levels with a fairly high data transfer speed.

IV. CONCLUSION

The development of a monitoring system to measure cholesterol and blood sugar levels has been successfully using the Nellcor DS-100A sensor based on the Blynk application. Equipment testing was carried out on 20 random samples by comparing prototype instruments and standard instruments (Autocheck 3-in-1). The results showed that the average accuracy of the prototype instrument to measure cholesterol and blood sugar level is 90.26% and 91.16%, respectively. It shows great potential in determining the estimation value at cholesterol and blood sugar levels. The monitoring system can show the data on the LCD display in Blynk Apps with the average time required of 1.07 s.

Acknowledgment

This work was supported by the financial aid from the DIPA BOPTN LP2M 2021, Universitas Islam Negeri Walisongo Semarang.

[1] L. J. Utama, "Gaya Hidup Mayarakat Nusa Tenggara Timur dalam Menghadapi Pandemi Corona Virus Disease 19 (Covid-19)," *Annada - Jurnal Kesehatan Masyarakat*, vol. 7, no. 1, pp. 34-40, 2020.

[2] T. Suryadin, S. Arhesa, and D. Febriana, "Gaya Hidup Sehat Masyarakat Desa Maja Selatan Pada Masa Pandemi Covid 19," *J. Educ.*, vol. 7, no. 3, pp. 657661, 2021.

[3] T. F. A. Atmadja et al., "Description of attitudes and healthy lifestyle of Indonesian community during pandemic Covid-19," *AcTion Aceh Nutr. J.*, vol. 5, no. 2, pp. 195202, 2020.

[4] M. Muslim, "Manajemen Stress pada Masa Pandemi Covid-19, *ESENSI J. Manaj. Bisnis*, vol. 23, no. 2, pp. 192201, 2020.

[5] R. Khan, "Postprandial blood glucose," *Diabetes Care*, vol. 24, no. 4, pp. 775778, 2001.

[6] D. R. Prasetyo, "Rancang Bangun Telemedicine Pengukur Kadar Kolesterol dalam Darah Berbasis Internet of Things," Tugas Akhir, Universitas Semarang, Semarang, Indonesia, 2019.

[7] W. F. Ramadhan, "Rancang Bangun Alat Ukur Detak Jantung Menggunakan Pulse Sensor Sen-11574 Berbasis Arduino Pro Mini Dengan Smartphone Android dan Oled SSD1306," Tugas Akhir, Universitas Islam Negeri Sunan Kalijaga, Yogyakarta, Indonesia, 2018.

[8] M. Elgendi, *PPG Signal Analysis: An Introduction Using MATLAB* (First Edit, Vol. 53, Issue 9). India: CRC Press, 2021.

[9] V. C. S. T. Sanders, "List of Boxes Clinical applications of the book s anatomical and physiological information are set apart from the text in boxed inserts and often deal with aspects of pathophysiology . A list of these boxes is presented here for your convenience," 2007.

[10] B. Tamarappoo et al., "Improvement in LDL is associated with decrease in non-calcified plaque volume on coronary CTA as measured by automated quantitative software," *Journal of Cardiovascular Computed Tomography*, vol. 12, no. 5. pp. 385390, 2018.

[11] K. Nishi et al., "Oxidized LDL in carotid plaques and plasma associates with plaque instability," *Arteriosclerosis, Thrombosis, and Vascular Biology*, vol. 22, no. 10. pp. 16491654, 2002.

[12] R. S. Dillon, "Importance of the hematocrit in interpretation of blood sugar.," *Diabetes*, vol. 14, no. 10, pp. 672674, 1965.

[13] R. Ekawita, A. A. Nasution, E. Yuliza, N. Suardi, and S. Suwarsono, "Development of Non-Invasive Blood Glucose Level Monitoring System using Phone as a Patient Data Storage," *J. Penelit. Fis. dan Apl.*, vol. 10, no. 2, p. 103, 2020.

[14] T. Nurmar'atin, H. Sumarti, and M. Ardhi, "Design and Implementation of Non-Invasive Telemedicine System for Detecting Cholesterol Levels in Blood as a Solution during the Covid-19 Pandemic," *Adv. Eng. Res.*, vol. 211, *Int. Conf. Sci. Eng.* (ICSE-UIN-SUKA 2021) Des., vol. 211, pp. 8691, 2021.

[15] G. Ndruru, R. E., Situmorang, M. and Tarigan, "Analisa Faktor-Faktor Yang Mempengaruhi Hasil Produksi Padi di Deli Serdang," *Saintia Mat.*, vol. 2, no. 1, pp. 7183, 2014.

[16] L. Agustine,i. Muljono, P.R. Angka, A. Gunadhi, D. Lestariningsih, W.A. Weliamto, "Heart Rate Monitoring Device for Arrhythmia Using Pulse Oximeter Sensor Based on Android," in *2018 International Conference on Computer Engineering, Network and Intelligent Multimedia, CENIM*, Surabaya, Indonesia, 2018, pp. 106-111.

[17] A. Microspheres, J. Prasad, A. Joshi, R. D. Jayant, and R. Srivastava, "Cholesterol Biosensors Based on Oxygen Sensing," *Biotechnol. Bioeng.*, vol. 108, no. 9, pp. 20112021, 2011.

[18] V. Semwal and B. D. Gupta, "LSPR- and SPR-Based Fiber-Optic Cholesterol Sensor Using Immobilization of Cholesterol Oxidase over Silver Nanoparticles Coated Graphene Oxide Nanosheets," *IEEE Sens. J.*, vol. 18, no. 3, pp. 10391046, 2018.

[19] S. Mukherjee, H. Raghuraman, and A. Chattopadhyay, "Membrane localization and dynamics of Nile Red: Effect of cholesterol," B*iochim. Biophys. Acta*, vol. 1768, pp. 5966, 2007.

[20] A. Mason, *Sensing Technology: Current Status and Future Trends IV*. New York: Springer Cham Heidelberg, 2015.

[21] X. Zhang, J. Chen, J.H. Yeo, "Blood sugar monitoring with laser diode," in *Proceedings Volume 6047, Fourth International Conference on Photonics and Imaging in Biology and Medicine*, 2006, p. 604741.

[22] K. Song, U. Ha, S. Park, J. Bae, H.-J. Yoo, "An Impedance and Multi-Wavelength Near-Infrared Spectroscopy IC for Non-Invasive Blood Glucose Estimation," *IEEE J. Solid-State Circuits*, vol. 50, no. 4, pp. 10251037, 2015.

[23] G Santoso, S Hani, S. Kristiyana, Y.A. Saputra, "Design Non-Invasive of Blood Sugar Detector Prototypes Using Cellular Technology GPS-Based," in J*Journal of Physics: Conference Series*, 2019, Madiun, Indonesia, vol. 1381, p. 012032.

[24] C. A. Vanstone, M. Raeini-sarjaz, W. E. Parsons, and P. J. H. Jones, "Unesterified plant sterols and stanols lower LDL-cholesterol concentrations equivalently in hypercholesterolemic persons 1 3," *Am J Clin Nutr*, vol. 76, pp. 12721278, 2002.

[25] M. S. Sandhu et al., ”LDL-cholesterol concentrations: a genome-wide association study,” *Nutr. Metab. Cardiovasc. Dis.*, vol. 371, pp. 483491, 2008.

[26] W. B. Baker, A. B. Parthasarathy, D. R. Busch, R. C. Mesquita, J. H. Greenberg, and A. G. Yodh, ”Modified Beer-Lambert law for blood flow,” *Biomed. Opt. Express*, vol. 5, no. 11, pp. 44074424, 2014.

[27] W. Lösche, F. Karapetow, A. Pohl, C. Pohl, T. Kocher, ”Plasma lipid and blood glucose levels in patients with destructive periodontal disease,” *J. Clin. Periodontol.*, vol. 27, no. 8, pp. 537-541, 2000.

[28] M. Sulehu and A. H. Senrimang, ”Program Aplikasi Alat Pengukur Kadar Glukosa Dalam Darah Non Invasive Bebasis Desktop,” *Inspir. J. Teknol. Inf. dan Komun.*, vol. 8, no. 1, pp. 1624, 2018.

[29] H. Suyono and Hambali, ”Perancangan Alat Pengukur Kadar Gula dalam Darah Menggunakan Teknik Non-Invasive Berbasis Mikrokontroler Arduino Uno,” *JTEV (Jurnal Tek. Elektro dan Vokasional)*, vol. 06, no. 01, pp. 6976, 2020.

[30] I. Marhaendrajaya, E. Hidayanto, and Z. Arifin, ”Desain dan realisasi alat pengukur kandungan kolesterol dalam darah non-invasive,” Y*oungster Phys. J.*, vol. 6, no. 3, pp. 290295, 2017.

JFA (JURNAL FISIKA DAN APLIKASINYA) VOLUME 18, NUMBER 3, OCTOBER 2022

The Metallicity of the Sun Reviewed from Pre-Main Sequence Evolution

Putri Indriani[1] and Aprilia*[2]

[1]Master Program in Astronomy, Faculty of Mathematics and Natural Sciences, Institut Teknologi Bandung, Jl. Ganesha No. 10, Bandung 40132, West Java, Indonesia
[2]Department of Astronomy, Faculty of Mathematics and Natural Sciences, Institut Teknologi Bandung, Jl. Ganesha No. 10, Bandung 40132, West Java, Indonesia

Abstract: Metallicity is defined as the fraction of the abundance of elements heavier than hydrogen and helium. Metallicity has different values for different stellar objects and its value will also change as the star evolves. This research is focused on calculating and analyzing the early metallicity of the Sun, that is at the beginning of the Sun's evolution at the Pre-Main Sequence. Five metallicity samples with an initial mass of 1 $M_\odot$ were used. This study uses the evolution code MESA r-15140 which produces a Hertzsprung-Russell diagram with various metallicities. From the simulation, it is found that the most suitable metallicity is 0.065. There are four dominant elements at the core of the Sun, namely hydrogen, helium, carbon, and oxygen. The density, pressure, and temperature values at the core of the Sun also increase with age.

Keywords: Metallicity; Sun; Pre-Main Sequence Evolution; MESA

*Corresponding author: aprilia@as.itb.ac.id

Article history: Received 15 April 2022, Accepted 26 September 2022, Published Oktober 2022.
http://dx.doi.org/10.12962/j24604682.v18i3.12791

I. INTRODUCTION

Metallicity is a fraction of the abundance of the heavier elements than hydrogen and helium which can be symbolized by Z, while hydrogen and helium are usually symbolized by X and Y. The relationship between these three abundance parameters is

$$X + Y + Z = 1 \tag{1}$$

Each star has a different metallicity value. The environment in which a star is formed is one of the important factors that determine the metallicity of a star. The metallicity value of a star is not constant, Z will change as the star evolves. Several methods can be used to calculate the Z value, among others are from photospheric spectroscopy observations, helioseismology, and observations of the solar wind. It can be reviewed from [1] some values obtained for the solar metallicity, among others are 0.0202 from spectroscopic observations of the Sun, 0.0245±0.001 from helioseismology using the abundance of the helium, and 0.0196±0.0014 from the measurement of heavy particles of the solar wind using a *Solar Wind Ion Composition Spectrometer*.

During their lives, stars experienced some evolution phases. Generally, it is divided to three main phases, namely Pre-Main Sequence, Main Sequence, and post Main Sequence phases. Our research will focus on the evolution of the Sun from the Pre-Main Sequence phase to its present phase as a Main Sequence star due to the changing in metallicity with the course of evolution. Star formation starts from interstellar clouds or interstellar medium (ISM) which has a very low density, very large volume, and very light mass. At the beginning of star formation, gravity plays a very important role. When there is a disturbance, the ISM will compress and the outside of the ISM will be pulled inward by gravity, this process is called condensation. The disturbance possibly come from shock waves from a supernova explosion or a collision with another cloud. The condition that must be met for a star to condense is to have a mass limit called the *Jeans* mass. Clouds with a mass greater than *Jeans* mass will not be able to maintain hydrostatic equilibrium and will shrink. Then there will be fragmentation, the cloud splits into many smaller pieces and each cloud undergoes gravitational shrinkage until the star temperature becomes high enough and becomes a protostar. This is where we start the Pre-Main Sequence phase.

The evolution of stars is usually depicted on the Hertzsprung-Russell (HR) diagram. The vertical axis in this diagram represents the luminosity value and the horizontal axis represents the effective temperature value which increases to the left. At first, when the Sun was still a protostar, its temperature and luminosity were still very low. At this low temperature, hydrogen is found in the form of H_2 molecules. Due to the pressure and collisions between molecules that occur more frequently, the temperature increases. There is an important line in the HR diagram, namely the Hayashi line/track, which marks a star in a state of perfect convection when it was in the Pre-Main Sequence evolution phase. Protostars that do not have a sufficiently high temperature and cannot maintain their hydrostatic equilibrium cannot cross this line, so they cannot continue their evolution to the next stage. The area of protostars before they cross the Hayashi line is called the Hayashi forbidden zone. The Sun, which was still

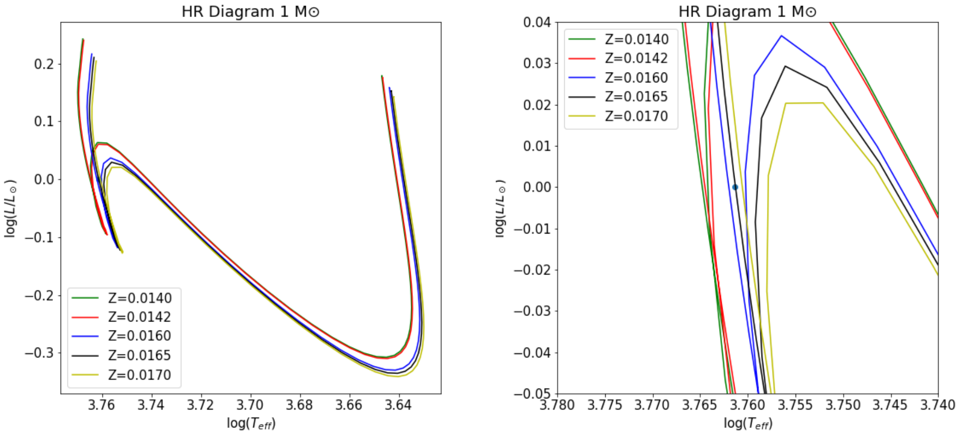

(a)

(b)

FIG. 1: (a) Pre-Main Sequence phase of the Sun on the HR diagram. Each line represents different metallicity: 0.0140, 0.0142, 0.0160, 0.0165, 0.0170. (b): We zoom in the image (a) to show the track with suitable metallicity for the Sun. The blue dot is the reference point for the Sun's current location on the HR diagram with $\log L/L_{\odot} = 0$ and $\log T = 3.7613$ [2].

a protostar, must be able to cross the Hayashi line to continue its evolution.

Protostars that follow Hayashi track still have low temperatures so that almost all stars are in a convective state. The temperature of the star will keep getting hotter so that the center of the star will be in radiative equilibrium. As more energy is transported radiatively, the luminosity and temperature of the star will also increase. At this stage, the evolutionary rate is much slower, and the convective envelope decreases with the increase in the radiative core. Contractions in protostars continue, according to the virial theorem, until the central temperature becomes high enough for hydrogen combustion to occur. When the hydrogen burns and fusion energy is generated, the star stops contracting and evolves into a star starting at the *Zero Age Main Sequence* (ZAMS) point which also marks the start of the evolutionary phase in the Main Sequence. At present, the Sun is still in this Main Sequence phase, with a luminosity of $L = 3.828 \times 10^{26} W$ and an effective temperature, $T = 5772K$ [2].

In this study, the metallicity will be determined based on the reference data of the current solar parameters and analyzed for temperature, pressure, and density. Part two of this article describes the research method, followed by the results and analysis in part three, and conclusions in part four.

II. RESEARCH METHOD

To determine the most suitable metallicity for the current state of the Sun, a modeling of the evolution of the star from the Pre-Main Sequence phase is carried out, assuming the Sun's initial mass is the same as the current mass of 1 $M_{\odot}$, with five metallicity values. The current position of the Sun on the Main Sequence, with luminosity and effective temperature values of $3.828 \times 10^{26} W$ and 5772 K, is used as a reference to obtain an evolutionary track that corresponds to the metallicity value used in the model.

The instrument used in this study is *Modules for Experiment in Stellar Astrophysics release* 15140 (MESA r-15140). MESA is an open-source 1D stellar evolution code which is regularly updated (see [3] for the latest updated version). With some input parameters needed in modeling the evolution of stars, we then obtain 53 related parameters which can be processed and analyzed further. In our model, as the input parameters, we have stellar mass, metallicity, and convective coefficient. From the output of the modelling, we analyze some parameters, such as effective temperature, luminosity, abundance of elements resulted from the fusion reactions in stellar center, age of the star during the evolution, and other parameters of the stellar center (density, temperature, pressure) to explain further about the evolution of the Sun.

III. MESA R-15140 INPUT

The MESA r-15140 provides a variety of inputs that can be tailored to fit each need. In this study, the input parameters are stellar mass $M = M_{\odot}$ (solar like star) as the initial mass of the Sun, metallicity values $Z = 0.0140, 0.0142, 0.0160, 0.0165, 0.0170$ (there are some values suggested as the solar metallicities (see [1] and references in)), and convective coefficient α_{MLT}, which is a parameter used to describe convection phenomena on the Sun, is 1.8 [4].

IV. RESULTS AND DISCUSSION

The metallicity of the Sun in the Pre-Main Sequence phase is different from the metallicity in the Main Sequence. There

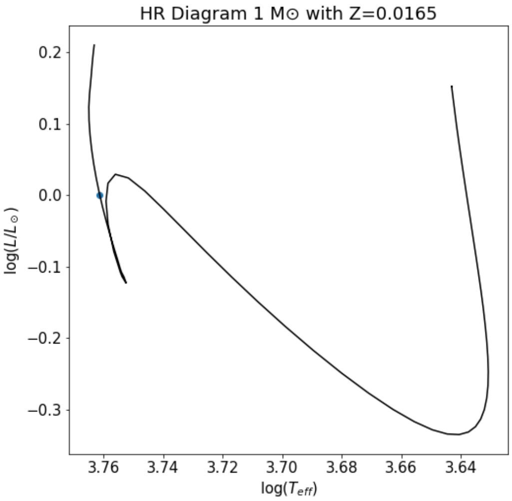

FIG. 2: Pre-Main Sequence phase of the Sun on the HR diagram for $Z = 0.0165$.

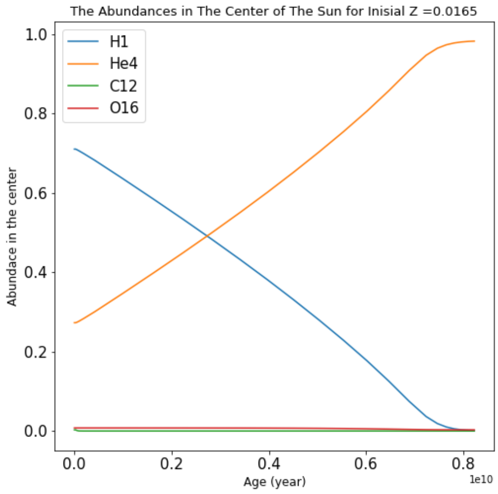

FIG. 3: The changes of chemical elements abundances at the center of the Sun with time.

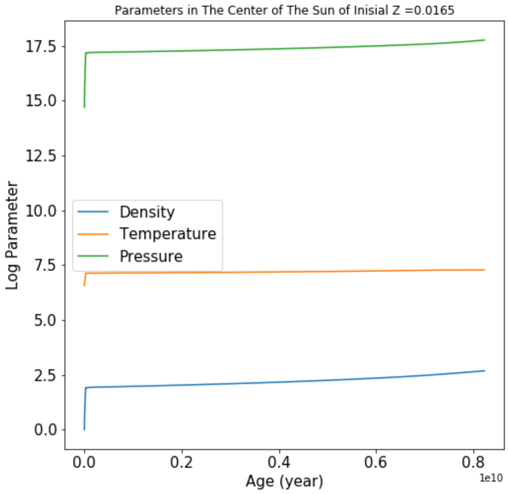

FIG. 4: The changes of density, temperature, and pressure at the center of the Sun during the Pre-Main Sequence phase.

are two candidates of metallicity values of the Sun when it was still a protostar, namely $Z_{protostar} = 0.0142$ [1] and 0.0140 [5]. From these two values, the HR diagram for the Sun is obtained (Fig. 1(a)).

In Fig. 1(a), we found that there is no line either from $Z_{protostar} = 0.0140$ (black line) or 0.0142 (red line) that passes the Sun's current reference point. Therefore, we perform an analysis using several metallicities to obtain a line that passes through the reference point by using the other metallicities namely 0.0160, 0.0165, and 0.0170. From these metallicities, we found that $Z_{protostar} = 0.0165$ is suitable as a candidate for the metallicity of the Sun in the Pre-Main Sequence phase because the graph in the HR diagram passes through the reference point.

By using the parameters mentioned in section 3 with $Z_{protostar} = 0.0165$, we get the Sun evolutionary track on the HR diagram in Fig. 2, starts from the Pre-Main Sequence phase, after crossing the Hayashi line from the Hayashi forbidden zone which is depicted to the zone with both very low effective temperature and luminosity (at the low left of the Fig. 2), to the end of Main Sequence phase. The protosun then traced Hayashi line vertically. At this time, the luminosity of the protosun decreased with a relatively constant temperature.

The modeling results also provide information about changes in the abundance of elements in the core of stars during evolution. This abundance depends on nuclear combustion that occurred during evolution. Fig. 3 shows the evolution of elemental abundance in the core of the Sun.

Four elements were produced in this modeling, namely hydrogen, helium, carbon, and oxygen. From Fig. 3, it can be seen that only hydrogen and helium underwent significant changes.

At the beginning of its age, the Sun was dominated by hydrogen. Due to the contraction that occurred while as a protosun, the temperature in the Sun's core increased, resulting in the burning of deuterium. The abundance of helium increases with the combustion of deuterium. This is shown in Fig. 3 that the abundance of helium increases with the decrease of hydrogen. With the burning of deuterium in its core, the temperature of the protosun also increased. Before reaching the Main Sequence, all deuterium had been converted to helium, and by the time the core temperature reached $T_{center} \sim 1.38 \times 10^7$ K, the protosun started the hydrogen burning reaction and marked the beginning of the Main Sequence phase of evolution.

Other parameters at the center of the Sun also underwent changes during the Pre-Main Sequence evolution phase. This is shown in Fig. 4 for the changing of the density, temperature, and pressure.

The values of these three parameters increase with the age of the Sun. The gradients of the three graphs also have different steepness, with density and pressure having greater steepness than temperature. These are related to convection events that occur in the Sun, especially when the protosun follows the Hayashi line downwards. The Sun is in the adiabatic phase [6] which can be showed from the ideal gas equation,

$$\nabla = \nabla_{ad} \tag{2}$$

$$P = K\rho^{\frac{5}{3}} \tag{3}$$

The temperature of the protosun, when it followed the Hayashi track, only experienced a much smaller increase in pressure and density. Deuterium combustion caused a rapid increase in density, followed by a rapid increase in central pressure. This increase continued until the protosun reached the Main Sequence phase.

V. CONCLUSION

From the Sun's current luminosity and temperature, we found that the most suitable metallicity for the Sun in the Pre-Main Sequence phase is 0.0165. This metallicity will increase with the increasing age of the Sun. This increase is directly related to the evolution of the abundance of elements present in the Sun. From the modeling we made, there are four most dominant elements in the evolution Sun from pre to the end of Main Sequence phase, namely hydrogen, helium, carbon, and oxygen. The density, temperature, and pressure also change during the evolution of the Sun. All three increase with age with different gradient slopes.

Acknowledgment

We thank to ITB for supporting this work as part of research project in master program in astronomy.

[1] S. Vagnozzi, "New Solar Metallicity Measurements," *Atoms*, vol. 7, issue 2, April 2019.

[2] A. Prša *et al.*, "Nominal Values for Selected Solar and Planetary Quantities: IAU 2015 Resolution B3," *The Astronomical Journal*, vol. 152, pp. 4147, August 2016.

[3] B. Paxton *et al.*, "Modules for Experiments in Stellar Astrophysics (MESA): Pulsating Variable Stars, Rotation, Convective Boundaries, and Energy Conservation," *The Astrophysical Journal Supplement Series*, vol. 243, issue 1, July 2019.

[4] J. Choi *et al.*, "Mesa Isochrones and Stellar Tracks (Mist). I. Solar-Scaled Models," *The Astrophysical Journal*, vol. 823, no. 2, p. 102, June 2016.

[5] H. S. Wang *et al.*, "The Volatility Trend of Protosolar and Terrestrial Elemental Abundances," *Icarus*, vol. 328, pp. 287305, 2019.

[6] F. Spada *et al.*, "Improved Calibration of the Radii of Cool Stars Based on 3D Simulations of Convection: Implication for the Solar Model," *The Astrophysical Journal*, vol. 868, no. 2, p. 135, December 2018.

JFA (JURNAL FISIKA DAN APLIKASINYA) VOLUME 18, NUMBER 3, OCTOBER 2022

Analysis of Vegetation Density and Surface Temperature in Buahbatu District, Bandung using Landsat 8 Oli/Tirs Satellite Images

Riki Purnama Putra*,[1] Rena Denya Agustina,[1] Khansa Qurratu'Aini,[1] and Kanya Adwasyifa[1]

[1]Program Studi Pendidikan Fisika, Fakultas Tarbiyah dan Keguruan, UIN Sunan Gunung Djati Bandung. Panyileukan, Jl. Cimencrang, Kec. Gedebage, Kota Bandung, Jawa Barat. 40292, Indonesia

Abstract: Urban Heat Island is a phenomenon of increasing temperature that occurs in the city area compared to the surrounding area. Urban Heat Island is caused by reduced vegetation due to changes in rural land use to urban areas. This study was conducted to analysis the relation between vegetation density (NDVI) and surface temperature (LST) in Buahbatu District as an effort to control the impact of the Urban Heat Island phenomenon. This research was conducted by processing data from Landsat 8 OLI/TIRS satellite images in 2019-2020, namely from May to October 2019 and May to October 2020. Data collection was carried out through Google Earth Engine to retrieve geospatial data visualization (satellite imagery) and USGS to download Landsat 8 satellite imagery on Bands 4 and 5, then the data is processed using Arcmap, and Pearson correlation test is performed on SPSS. The results obtained are a correlation between vegetation density and surface temperature. In Buahbatu District, the correlation between vegetation density and surface temperature shows a value of (-.403*) in 2019 and (-.386*) in 2020. Both show a negative correlation, which means that if an area has high vegetation density, the surface temperature will decrease, and vice versa. In addition, Buahbatu District gets a good UHI with an NDVI above 0.25, and an LST below 30 but not less than 25.

Keywords: NDVI; Land Surface Temperature; LST; Urban Heat Island

*Corresponding author: purnamariki20@gmail.com

Article history: Received 11 April 2022, Accepted 15 September 2022, Published October 2022.
http://dx.doi.org/10.12962/j24604682.v18i3.12739
2460-4682 ©Departemen Fisika, FSAD-ITS

I. INTRODUCTION

The city of Bandung is a city surrounded by mountains, so it forms like a basin. Bandung city has generally cool air, which means it has low temperature. In 2012 it was recorded that the highest temperature in Bandung was 30.9°C, which happened in September. Meanwhile, the lowest temperature in Bandung reached 17.4° C, recorded in July [1, 2]. However, it cannot be denied that several areas of Bandung City have warmer and even hotter temperatures than other cities, for example, Bogor City. The phenomenon of rising temperature in Bandung City is closely related to the Urban Heat Island (UHI) phenomenon or Urban Heat Island, where an urban area has a higher temperature than the surrounding areas [3, 4]. One of the reasons that cause this phenomenon is the high urbanization in Bandung city [5] that eventually leads to UHI and will negatively affect health, energy, and food. According to the U.S. Environmental protection Agency (2014) [6], the influence of urban heat islands in urban areas can affect the environment and quality of life of the community, increase air pollution emissions and the presence of greenhouse gases, which can affect the comfort of living in the city and can endanger health [7].

Among the factors that cause UHI in Bandung is the change in land use from rural to urban areas. These rural areas are generally used as agricultural land and forests. This change in land use from rural to urban areas causes a decrease in vegetation in the area of Bandung City [5]. Vegetation is an assemblage of plants in one place, including the vegetation structure, vegetation proportion, and diversity of green plants that function as land cover, reducing surface runoff and maintaining soil temperature [8]. Therefore, it is necessary to research the effect of vegetation density on surface temperature as an effort to control the impact of UHI. UHI is very important to note because UHI is very influential on the level of heat in an area for sustainable development [9]. An urban place that is very hot will certainly not be an effective place for sustainable development. In accordance with previous research which stated that UHI is the most important component in sustainable development because UHI is the beginning of an analysis of the direction of development that will be developed in an area [10]. In addition, previous research stated that sustainable development must have clear directions and goals, with UHI data presented in the form of the Normalized Difference Vegetation Index (NDVI) and Land Surface Temperature (LST) [11]. It is possible to relocate residential areas by looking at UHI as the initial basis for whether the place to be relocated can meet the climate requirements for residents or not [12]. UHI in urban areas, of course, can focus on housing development which is useful if you want to become a green city by installing solar panels in every house. This study aims to analyze NDVI (Normalize Vegetation Index) and LST (Land Surface Temperature) which focuses on Buahbatu District, Bandung City.

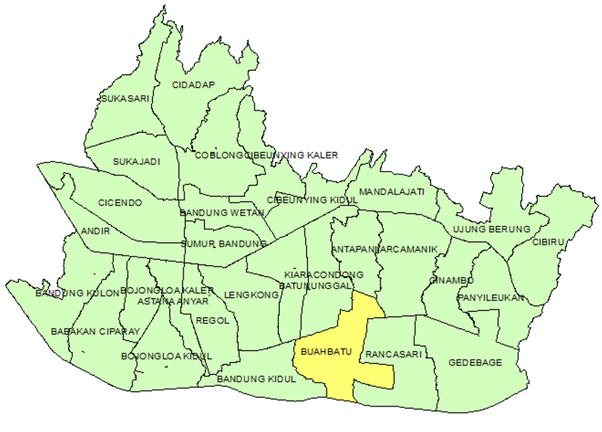

FIG. 1: Study Area

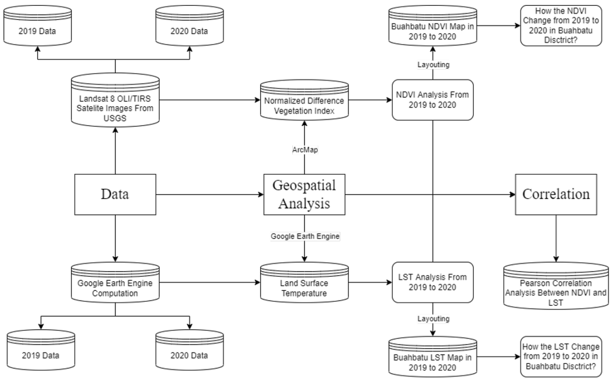

FIG. 2: Research Flowchart

Of course, this research will help sustainable development in the form of initial analysis of development, especially in the Buahbatu disctrict of Bandung City.

II. METHOD

This research was conducted in Buahbatu district, one of the districts in the City of Bandung, West Java. The Buahbatu district has a total area of .814 Ha. The surface elevation of Buahbatu District is 500 m above sea level, with 75 percent of the land being flat and choppy. Administratively, the boundaries of the Buahbatu District are: 1) In the south it is bounded by the District of Bojong Soang; 2) In the north it is bounded by the District of Kiaracondong and Antapani; 3) In the east it is bounded by the Rancasari district, Bandung; 4) In the west, it is bounded by Bandung Kidul district, Bandung, as shown in Fig. 1.

This research was conducted by processing Landsat Thermal Infrared Sensor (TIRS) 8 data in 2019-2020 using a technique in the form of image data, applied to compile the distribution of greenery levels and their correlation with temperature distribution. As in flowchart, this research can be explained in Fig. 2.

TABLE I: Correlation Interpretation

No	r value	Interpretation
1	0.00-1.199	Very Low
2	0.20-0.399	Low
3	0.40-0.599	Middle
4	0.60-0.799	Strong
5	0.80-1.000	Very Strong

The research media used are ArcMap, Google Earth Engine, and USGS, which are used to obtain geospatial data in the form of satellite images from remote sensing results. Data collection was carried out from May 2019 to October 2019 and May 2020 to October 2020.

The research process was first carried out by searching for surface temperature data, obtained through the Google Earth Engine by entering specific code using the Java programming language. Temperature data was obtained through Landsat 8 OLI/TIRS C1 imagery level 1 Band 4, 5, 10, and 11. Then the data is processed through ArcMap to know the distribution of the surface temperature.

The following process looks for NDVI (Normalized Difference Vegetation Index) data by first downloading the Landsat 8 OLI/TIRS C2 L2 image data on the available USGS. Furthermore, the data is processed using ArcMap to obtain vegetation density data. The equation used in the NDVI calculation can be seen on Eq. 1.

$$NDVI = \frac{PIR - R}{PIR + R} \tag{1}$$

And on Landsat 8, the equation becomes:

$$NDVI = \frac{B5 - B4}{B5 + B4} \tag{2}$$

Eq. 2 is a calculation of the vegetation index value, which is the measurement value of healthy vegetation. The vegetation index has a value range of -1 to 1. The NDVI -1 value indicates the state of the non-vegetated area and the NDVI 1 value indicates the maximum vegetation area.

To determine the relationship between NDVI, a correlation test was carried out between NDVI (Normalized Difference Vegetation Index) and LST (Land Surface Temperature) through ArcMap and Pearson correlation test on SPSS. The interpretation of the correlation can be seen in Table I [13].

III. RESULTS AND DISCUSSION

Normalized Difference Vegetation (NDVI) or Vegetation Index is data obtained through a mathematical approach based on the reflection of the vegetation canopy in the form of a comparison between the brightness levels of the red band and near infrared band [4]. Vegetation is an assemblage of plants in one place, including vegetation structure, the proportion of vegetation, and the diversity of green plant species that function as land cover [8].

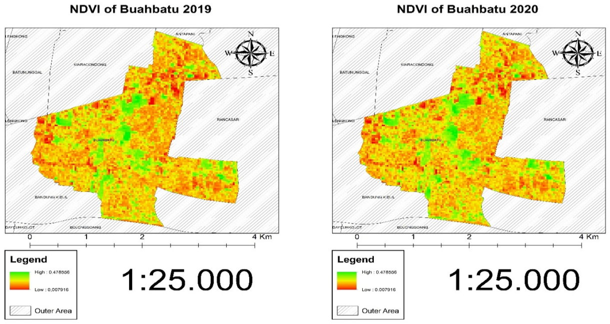

(a) (b)

FIG. 3: NDVI of Buahbatu District from (a) May to October 2019 and (b) May to October 2020.

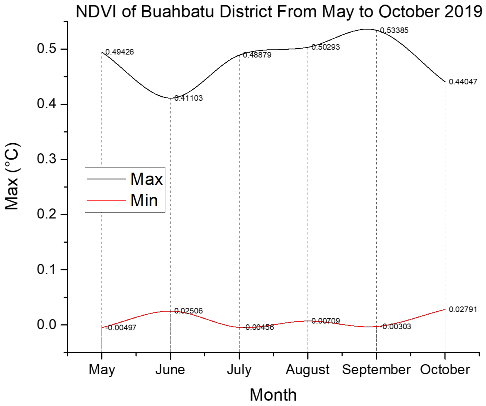

FIG. 4: NDVI Graph of Buahbatu District from May to October 2019.

According to research by Wachid [14], plants can emit or absorb radiation waves emitted to distinguish between vegetation and non-vegetation. According to Sagita [15], non-vegetation areas are residential areas, water areas, vacant lands, and areas with very low vegetation index, will have a minimum ratio of the red band and near infrared band ratio values. Meanwhile, for areas with very dense vegetation, green, and healthy vegetation conditions, the ratio of the comparison value of the red band and near infrared band will be maximum.

The ratio of the red band and near infrared band values is the normality value of the vegetation index or NDVI. According to Mabrur [16], the equation for calculating the NDVI value can be seen on Eq. 1, and the average temperature in 2019 and 2020 in Buahbatu sub-district with a period from May to October can be seen in Fig. 3.

NDVI data from the result of Landsat 8 OLI/TIRS C2 L2 image procession using ArcMap can be seen in Table II.

The vegetation index shown in Table II shows various values. It also show vegetation density from May to October 2019. The maximum values show the highest vegetation density in the Buahbatu district area. Meanwhile, the minimum values indicate the lowest vegetation density in the Buahbatu district area.

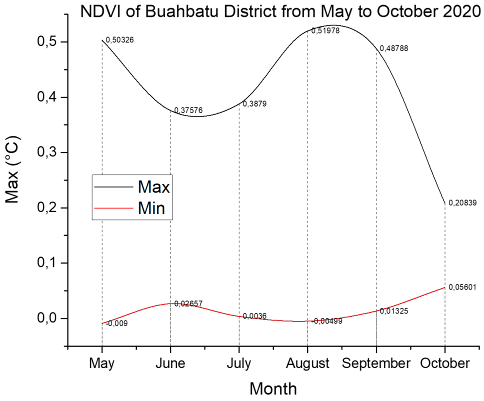

FIG. 5: NDVI Graph of Buahbatu District from May to October 2020.

TABLE II: NDVI of Buahbatu District from May to October 2019

Month	NDVI	
	Max	Min
May	0.49426	-0.0049718
June	0.411034	0.025059
July	0.488785	-0.00456
August	0.502931	0.007087
September	0.533854	-0.00303
October	0.440472	0.027911
Mean	0.478556	0.007916

TABLE III: NDVI of Buahbatu District from May to October 2020

Month	NDVI	
	Max	Min
May	0.503263	-0.009
June	0.375762	0.0265722
July	0.387902	0.0036007
August	0.519783	-0.0049887
September	0.48788	0.0132469
October	0.208391	0.0560087
Mean	0.4138302	0.01424

Table II also shows the level of vegetation density in the Buahbatu district in 2019, with the highest vegetation density level shown in September with the maximum vegetation density being 0.533854 and the lowest vegetation density being -0.00303. Based on the data in Table II, the average value of vegetation density in Buahbatu District is in the range of 0.478556 and 0.007915. This shows that the district of Buahbatu has a fairly high level of vegetation considering that the vegetation range is in the value of -1 to 1.

The level of vegetation density in the Buahbatu district in 2020 is shown in Table III. The highest vegetation density level is shown in August, with a maximum vegetation density of 0.519783, with the lowest vegetation density level being -0.00498866. Based on the data in Table II and III, the

TABLE IV: The Surface Temperature of Buahbatu District from May to October 2019

Month	**Temperature (°C)**	
	Max	**Min**
May	32.3991	24.3891
June	32.9592	24.5103
July	34.341	24.6033
August	35.264	23.9705
September	34.8223	25.2572
October	37.7044	26.6919
Mean	34.58167	24.90371

TABLE V: The Surface Temperature of Buahbatu District from May to October 2020

Month	**Temperature (°C)**	
	Max	**Min**
May	28.4528	22.3265
June	28.3206	22.1887
July	28.3359	22.0976
August	27.1824	21.3101
September	27.4158	21.3735
October	27.1824	21.3101
Mean	27.8149	21.76775

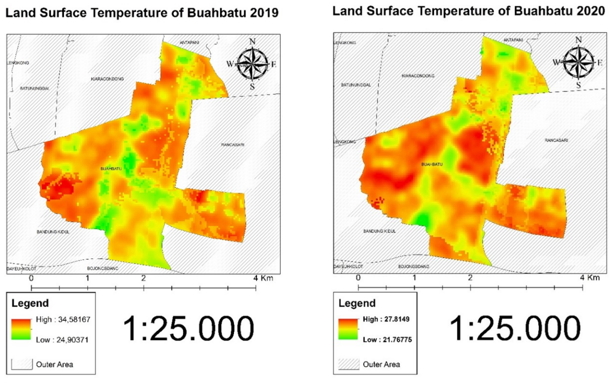

(a) (b)

FIG. 6: Land Surface Temperature of Buahbatu District from (a) May to October 2019 and (b) May to October 2020.

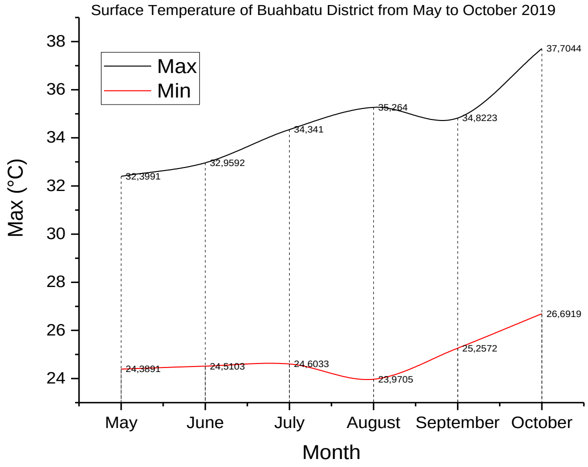

FIG. 7: Graph of Surface Temperature of Buahbatu District from May to October 2019.

average value of vegetation density in Buahbatu District is in the range of 0.413830167 and 0.014239975. The vegetation index of Buahbatu District in 2020 also showed a reasonably high value, similar to the vegetation index of Buahbatu District in 2019.

Fig. 5 shows the NDVI graph from May to October 2020. Based on the graph, the level of vegetation density in Buahbatu District has decreased and increased repeatedly, the same as in 2019. The highest vegetation density level was in August, which was 0.519783. The lowest vegetation level was in May, which was -0.009.

Land Surface Temperature (LST) is defined as the temperature of the outermost part of an object and the first element that can be defined from thermal satellite images and described in pixels with various types of surfaces. The average temperature in 2019 and 2020 in Buahbatu sub-district with a period from May to October can be seen in Fig. 6.

From the surface temperature data conducted on Google Earth Engine and ArcMaps assisted by Landsat 8 OLI/TIRS satellite imagery, the average surface temperature results from the recording period from May to October 2019 and 2020 were obtained. The average surface temperature is considered the surface temperature that represents the year's temperature. Table IV is a table of surface temperatures from Land Surface Temperature (LST) data in 2019 as well as Fig. 7.

The surface temperature data shown in Table IV shows varied surface temperature results. The maximum temperature from May to October 2019 is in the range of 32-37°C. It continued to rise from May to August, and finally decreased in September, then rose again drastically in October. It is similar to the minimum temperature in 2019 when the value continued to increase from May to August, and finally decreased in September, then rose again drastically in October, as shown in the following graph in Fig. 7.

The graph in Fig. 7 shows that the maximum surface temperature in the Buahbatu area in 2019 was in October with a temperature value of 37.7044°C, and the minimum surface temperature in the Buahbatu area in 2019 was in May with a temperature value of 24.3891°C.

Furthermore, the 2020 surface temperature data in Table V gives a reasonably constant surface temperature result. The maximum temperature from May to October 2020 is in the range of 27-28°C, in contrast to 2019, which has a maximum temperature value difference up to 3°C.

Table V also shows that the Maximum Temperature value continued to decrease from May to August, and finally experienced a slight increase in September, then rose again in October. Similar to the Minimum Temperature in 2020, its value continued to fall from May to August, and finally experienced a slight increase in September, then rose again in October, as shown in the graph in Fig. 8.

Fig. 8 shows that the maximum surface temperature in the

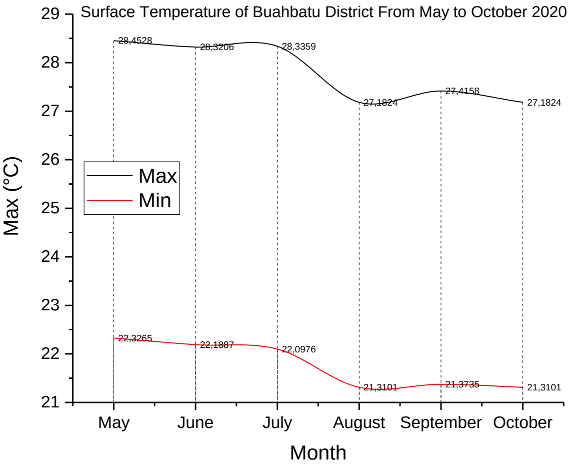

FIG. 8: Graph of Surface Temperature of Buahbatu District from May to October 2020.

Buahbatu area in 2020 was in May with a temperature value of 28.4528°C, and the minimum surface temperature in the Buahbatu area in 2020 was in October with a temperature value of 21.3101°C. Based on NDVI and LST data obtained from 2019 to 2020 in the Buahbatu District area, it shows that NDVI has not changed drastically, but there has been a decline in NDVI in 2020. In addition, LST in 2020 has decreased quite drastically. The results of the analysis on NDVI and LST from 2019 to 2020 that the Buahbatu district is considered feasible because the qualified NDVI is still at the level > 0.25 and the LST is at $25 < X < 30$. Based on the opinion expressed by previous researchers who stated that a good area to be used as a place of resettlement if the place has an NDVI of > 0.25, and an LST of not less than 25 and not more than 30 [17].

The presence of vegetation can reduce temperature because its surface absorbs some of the solar radiation energy and uses it to evaporate water from plant tissue (transpiration) and solid surfaces containing water (evaporation) [18]. Vegetation value is closely related to land surface temperature, proven by the Pearson analysis correlation test in 2019, which can be seen in Table VI.

According to Table VI, Pearson Correlation in 2019, vegetation density to surface temperature, the correlation coefficient value is -.403**. Based on the interpretation of the Pearson correlation, this value shows a moderate correlation because it is in the range of 0.40 to 0.599. The value -.403 also indicates a negative correlation between the vegetation index (NDVI) and surface temperature (LST). The negative correlation value proves that the two variables have an inverse relationship, indicating that the higher the vegetation index value, the lower the surface temperature.

The results of this correlation, as well as in the correlation test conducted in 2020, can be seen in Table VII. It shows that in 2020 Pearson correlation test is the same as the 2019 correlation test in Table VI. The correlation coefficient value in 2020 was -.386**, which shows a negative correlation between the vegetation index and surface temperature. As for the interpretation of the correlation level, it shows a weak correlation because the value is in between the range of 0.20 to 0.399.

TABLE VI: Pearson Correlations Analysis in 2019

Correlations			
		Land Surface Temperature (LST)	**Vegetation Density (NDVI)**
Land Surface Temperature (LST)	Pearson Correlation	1	-.403**
	Sig. (2-tailed)		.000
	N	7058	7058
Normalized Difference Vegetation Index (NDVI)	Pearson Correlation	-.403**	1
	Sig. (2-tailed)	.000	
	N	7058	7058

**. Correlation is significant at the 0.01 level (2-tailed).

TABLE VII: Pearson Correlations Analysis in 2020

Correlations			
		Land Surface Temperature (LST)	**Vegetation Density (NDVI)**
Land Surface Temperature (LST)	Pearson Correlation	1	-.386**
	Sig. (2-tailed)		.000
	N	6621	6621
Normalized Difference Vegetation Index (NDVI)	Pearson Correlation	-.386**	1
	Sig. (2-tailed)	.000	
	N	6621	6623

**. Correlation is significant at the 0.01 level (2-tailed).

In the 2019 and 2020, NDVI and LST correlation data, both show a Sig (2-tailed) of .000, which means that there is a correlation between NDVI and LST. The correlation data is also supported by research conducted by [19] and [20] that a lack of vegetation can affect surface temperature; when vegetation decreases, the surface temperature will increase.

IV. CONCLUSION

Based on the Pearson correlation test, it was found that there is a correlation between NDVI (Normalized Difference Vegetation Index) with LST (Land Surface Temperature), meaning that the level of vegetation in an area affects the surface temperature of the area. The research results obtained regarding the correlation of NDVI and LST in Buahbatu District in 2019 and 2020 show a correlation with the Pearson correlation value of (-.403*) in 2019 and (-.386*) in 2020. Both show a negative correlation. A negative correlation means that if one variable increases, the other variables will decrease, and vice versa. In the results obtained show the relationship between NDVI and LST is inversely. In other words, NDVI in Buahbatu District increased, then LST in Buahbatu District decreased. In addition, Buahbatu District is considered good for residential areas, because the NDVI result is > 0.25 and the LST is not more than 30 but not less than 25.

Acknowledgment

Authors are grateful to LP2M UIN Sunan Gunung Djati Bandung which has assisted in providing facilities so that this research can be carried out properly. In addition, we acknowledge Faculty of Tarbiyah dan Keguruan and Departement of Physics Education for supports in carrying out this research.

[1] BPS Provinsi Jawa Barat, ”Temperatur, Curah Hujan, dan Hari Hujan di Bandung, 2009-2014”, *Badan Pusat Statistik Provinsi Jawa Barat*, 2015.

[2] M. A. Priatna and E. C. Djamal, ”Precipitation prediction using recurrent neural networks and long short-term memory,”*Telkomnika (Telecommunication Comput. Electron. Control)*, vol. 18, no. 5, pp. 2525-2532, 2020.

[3] B. E. B. Dewantoro, P. A. Natani, and Z. Islamiah, ”Analisis Surface Urban Heat Island Menggunakan Teknik Penginderaan Jauh Berbasis Cloud Computing Pada Google Earth Engine Di Kota Samarinda,” *Semin. Nas. Geomatika*, no. October, p. 75, 2021.

[4] R. C. Zulkarnain, ”Pengaruh Perubahan Tutupan Lahan Terhadap Perubahan Suhu Permukaan di Kota Surabaya,” *Skripsi Inst. Teknol. Sepuluh Nop.*, 2016.

[5] F. Ihsan and D. Rosleine, ”Cooling effect to mitigate Urban Heat Island by Pterocarpus indicus, Swietenia macrophylla and Samanea saman in Bandung, West Java Indonesia,” *IOP Conf. Ser. Earth Environ. Sci.*, vol. 528, no. 1, 2020.

[6] U.S. Environmental protection Agency, ”2013 U.S. Environmental Protection Agency (EPA) International Decontamination Research and Development,” Durham, 2014.

[7] S. Kang, R. Yang, H. Ozer, and I. L. Al-Qadi, ”Life-cycle greenhouse gases and energy consumption for material and construction phases of pavement with traffic delay,” *Transp. Res. Rec.*, vol. 2428, no. 1, pp. 27-34, 2014.

[8] N. Maryantika, L. M. Jaelani, and A. Setiyoko, ”Analisa perubahan vegetasi ditinjau dari tingkat ketinggian dan kemiringan lahan menggunakan citra satelit Landsat dan Spot 4 (Studi kasus kabupaten Pasuruan),” *Geoid*, vol. 7, no. 1, pp. 098-100, 2011.

[9] K. Deilami, M. Kamruzzaman, and Y. Liu, ”Urban heat island effect: A systematic review of spatio-temporal factors, data, methods, and mitigation measures,” *Int. J. Appl. earth Obs. Geoinf.*, vol. 67, pp. 30-42, 2018.

[10] V. R. S. Cheela, M. John, W. Biswas, and P. Sarker, ”Combating urban heat island effectA review of reflective pavements and tree shading strategies,” *Buildings*, vol. 11, no. 3, p. 93, 2021.

[11] J. Peng *et al.*, ”How to effectively mitigate urban heat island effect? A perspective of waterbody patch size threshold,” *Landsc. Urban Plan.*, vol. 202, p. 103873, 2020.

[12] J. Yang, Y. Wang, C. Xiu, X. Xiao, J. Xia, and C. Jin, ”Optimizing local climate zones to mitigate urban heat island effect in human settlements,” *J. Clean. Prod.*, vol. 275, p. 123767, 2020.

[13] R. P. Putra, I. Ramadhanti, S. Andhika, R. D. Agustina, and P. Pitriana, ”Pengaruh Kecerdasan Emosional terhadap Literasi Digital Praktikum Virtual Fisika pada Sudut Pandang Gender Mahasiswa,” *WaPFi (Wahana Pendidik. Fis.)*, vol. 7, no. 1, pp. 46-51, 2022.

[14] N. Wachid and W. P. Tyas, ”Analisis Transformasi NDVI dan kaitannya dengan LST Menggunakan Platform Berbasis Cloud: Google Earth Engine,” *J. Planol.*, vol. 19, no. 1, pp. 60-74, 2022.

[15] A. R. Sagita, A. S. C. Margaliu, F. Rizal, and H. P. Mazzaluna, ”Analisis Korelasi Suhu Permukaan, NDVI, Elevasi dan Pola Perubahan Suhu Daerah Panas Bumi Rendingan-Ulubelu-Waypanas, Tanggamus Menggunakan Citra Landsat 8 OLI/TIRS,” *J. Geosains dan Remote Sens.*, vol. 3, no. 1, pp. 43-51, 2022.

[16] A. F. Mabrur, N. A. Setiawan, and I. Ardiyanto, ”Remote Sensing Technology for Land Farm Mapping Based on NDMI, NDVI, and LST Feature,” IJITEE *(International J. Inf. Technol. Electr. Eng.)*, vol. 3, no. 3, pp. 75-79, 2019.

[17] Y. Li, Y. Sun, J. Li, and C. Gao, ”Socioeconomic drivers of urban heat island effect: Empirical evidence from major Chinese cities,”S*ustain. Cities Soc.*, vol. 63, p. 102425, 2020.

[18] A. Priana, A. Nugroho, E. Purnamasari, M. Rais, and Y.A. Perlambang, ”The Pattern of Spatial Distribution of Agriculture Drought Using Landsat 8 OLI/TIRS in Bacukiki District, City of Parepare,” in *The 6th Geoinformation Science Symposium 2019*, p. 14, 2020.

[19] D. M. Indrawati, S. Suharyadi, and P. Widayani, ”Analisis Pengaruh Kerapatan Vegetasi Terhadap Suhu Permukaan dan Keterkaitannya Dengan Fenomena UHI,” *Media Komun. Geogr.*, vol. 21, no. 1, p. 99, 2020.

[20] M. Dede, G. P. Pramulatsih, M. A. Widiawaty, Y. R. R. Ramadhan, and A. Ati, ”Dinamika Suhu Permukaan Dan Kerapatan Vegetasi Di Kota Cirebon,” *Jurnal Meteorologi Klimatologi dan Geofisika*, vol. 6, no. 1, pp. 23-30, 2019.

JFA (JURNAL FISIKA DAN APLIKASINYA) VOLUME 18, NUMBER 3, OCTOBER 2022

Performance Analysis of Cone Basin-Based Gravitational Water Vortex Power Plant (GWVPP) by Variations in the Number of Blades

Iim Fatimah*,[1] Haswin Dian Fathoni,[1] and Bachtera Indarto[1]

[1]Department of Physics, Faculty of Science and Data Analytics, Institut Teknologi Sepuluh Nopember (ITS) Kampus ITS Sukolilo, Surabaya 60111, Indonesia

Abstract: The electricity supply is not evenly distributed for all regions in Indonesia. This is due to the lack of transportation access to reach these areas because of difficult terrain conditions. One of abundant energy sources available in nature is water, which can be used for micro-level power generation. Micro hydro generator usually uses a waterfall with a high head. However, not all of the water flow has a head tall. Therefore, this study proposes a promising prototype of a cone basin-based Gravitational Water Vortex Power Plant (GWVPP). The purpose of this study is to determine the performance of the cone basin-based GWVPP prototype by variation in the number of blades. The vortex turbine is designed with a water flow rate of 169.63 liters/minute and a cone basin with square-shaped blades and variations in the number of blades, namely 2, 4, and 6, with the same turbine blade area of 0.01 m^2. It was found that an increase in the number of blades enhances mechanical characteristics of, *e.g.* torque and rotational speed, as well as electrical characteristics, *e.g.* voltage, current, and electric power. The maximum result is achieved when the number of blades is six with the rated power of 5 mW and the rotation speed of 119.351 rpm.

Keywords: Gravitational Water Vortex; Number of Blades; Microhydro; Turbine Power

*Corresponding author: iim.fatimah.its@gmail.com

Article history: Received 30 September 2022, Accepted 31 October 2022, Published October 2022.
http://dx.doi.org/10.12962/j24604682.v18i3.14496

I. INTRODUCTION

Electricity is a source of energy commonly used by humans. Electricity is generated through a power generation system. The generators that are widely used are hydropower power plants, natural gas power plants, steam power plants, diesel power plants, and nuclear power plants. In general, steam and diesel power plants use energy sources in the form of coal or oil earth. Power plants utilize hydro-power as the main medium for propulsion turbine and generator. Technically, a micro-hydro generator has three main components, namely water as a source of energy for turbines and generators. Water flowing with a certain capacity is channeled by a certain height through a rapid pipe to the installation house (powerhouse) [1].

Energy has a very important role for the movement of the Indonesian economy. Among other energy user sectors, industry is the largest energy user sector, especially electrical energy. Not only used in the industrial sector, electrical energy is also used in household, political, and academic. In 2019, the General Plan for the Provision of Electricity (RUPTL) of the State Electricity Company (PLN) stated that it was only able to provide 57% of electrical energy from the total needs of the community [2]. This shows that the supply of electrical energy provided by PLN has not been able to meet the needs of the community. The lack of fulfillment of electrical energy in Indonesia can have an impact on several aspects such as economic, academic, political, and so on [3].

Considering those conditions, it is necessary to develop an alternative renewable energy. Indonesia has great potential for the development of renewable alternative energy, such as by utilizing geothermal energy, solar energy, wind, and water [4]. The role of renewable energy has been recognized as great significance for the global environmental concerns [5]. Hydro power is a good example of renewable energy, and its potential application to future power generation cannot be underestimated [6]. The Gravitational Water Vortex Power Plant (GWVPP) has the greatest potential at low-head sites among other hydro power technologies [7, 8].

In this study, to overcome the shortage of electrical energy in Indonesia, the authors conducted research in terms of the Microhydro Power Plant (MPP) system. One of the MPP systems currently being developed is the GWVPP by analyzing the effect of the number of blades on the turbine performance.

II. METHOD

The design of the turbine in this study was carried out in terms of the design of the turbine blade support pole height, the shape and area of the blade, and the number of turbine blades. For the height of the support pole of the turbine blade, due to adjustment to the height of the existing cone basin, the pile height is 80 cm. Furthermore, the determination of the

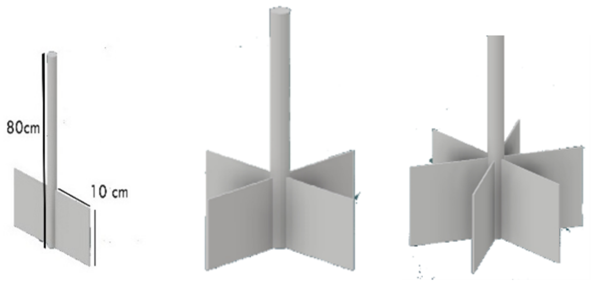

(a) (b) (c)

FIG. 1: Turbine blades design of (a) 2 blades, (b) 4 blades, (c) 6 blades.

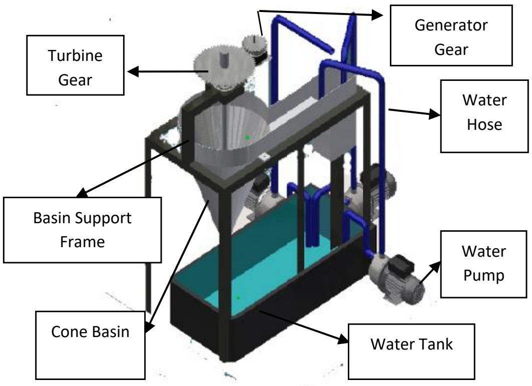

FIG. 2: Design of the cone basin-based Gravitational Water Vortex Power Plant (GWVPP) system.

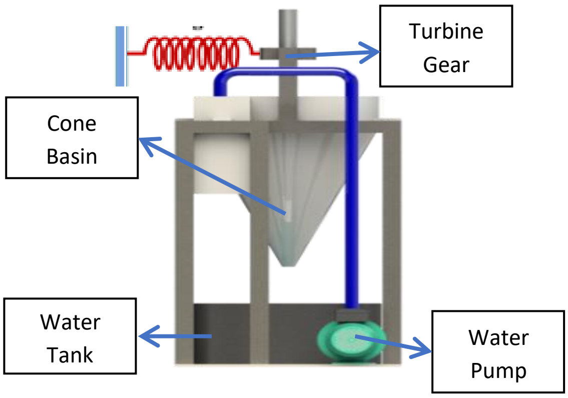

FIG. 3: Torque measurement scheme in a cone basin-based GWVPP.

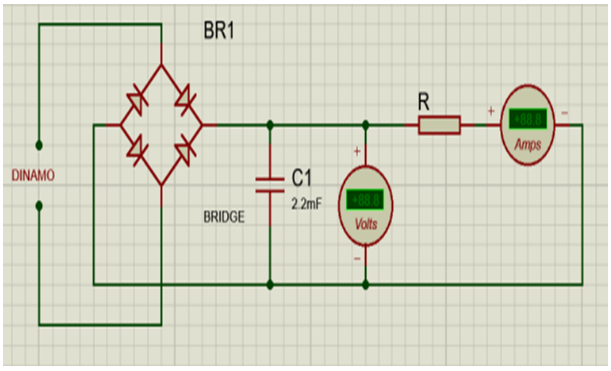

FIG. 4: The measurement circuit of voltage and current with a load resistor.

shape of the turbine blade from research that has been done previously obtained data that the best efficiency on the turbine is used with a straight blade shape with a square shape with a length of each side is 10 cm. The design of the number of turbine blades is determined by 3 variations in the number of vortex turbine blades, which is 2, 4, and 6. The blade design that will be used in the study is shown in Fig. 1. Meanwhile, the cone basin-based GWVPP system design is shown in Fig. 2.

Fig. 2 shows the measurement design of the tool, there are several components other than the turbine which include a basin with a cone shape that is used as a place for vortex formation. The water pump is used as a means of producing water flow, for example, the flow of river water. Water hose is employed as a water channel from the pump to the temporary water reservoir. The turbine gear is used to turn the generator gear. Gear generator is applied as a means of converting the rotation of the gear on the turbine so that later it can be converted into electrical energy. Falling water reservoirs are used for containers of water that fall from the cone out-late basin which will then be flowed continuously to a temporary reservoir by the available water pump.

Data collection begins with measuring the value of the water discharge generated by the tool system. With the use of a stopwatch as a time measurement tool, the rotational speed is obtained for every 60 rotations of the turbine gear. Meanwhile, the torque measurement is carried out using a circuit scheme as shown in Fig. 2 with the addition of a spring as a measuring instrument as shown in Fig. 3. The value of the spring constant used is 119.35 N/m. The data obtained in this study are in the form of torque and rotational speed generated by the turbine, voltage and current generated by the generator, and the total power value obtained by the whirlpool power plant. This study employs variations of the height of the turbine blades with variations in the depth of the turbine to the basin, namely 18, 20, 22, 24 and 26 cm.

The voltage and current were measured with load resistor. The circuit used is shown in Fig. 4. The measurement were performed with a number of resistor variations, 1, 3, 10 and 25 kΩ. Then the last data retrieval is the retrieval of electrical power data by using the current-voltage relationship.

III. RESULTS AND DISCUSSION

The data obtained in this study are the value of rotational, torque, electric current, and electric power. The rotational speed data shows that the largest value is owned by the vari-

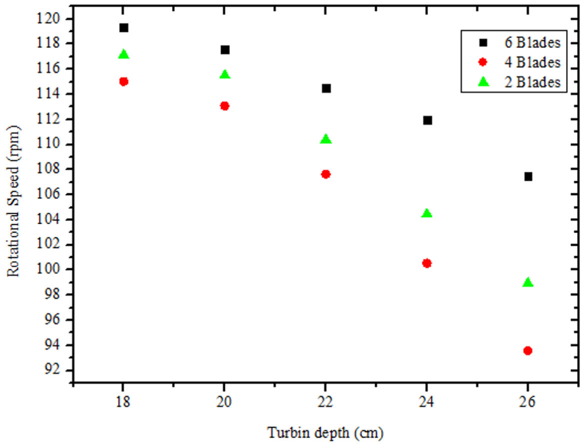

FIG. 5: The rotational speed of the GWVPP with different number of blades.

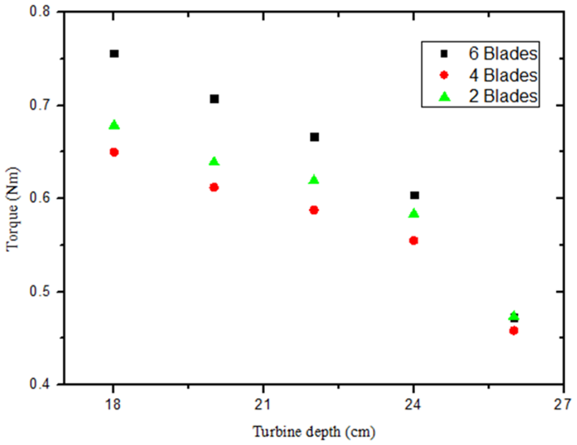

FIG. 6: The torque of the GWVPP with different number of blades.

ation of 6 turbine blades, followed by 2 and 4 turbine blades. The simulations carried out by Min Sung Kim, *et. al.* [9], reached a steady state after 2000 iterations, even if run further, up to 5000 iterations. Torque variation is thought to be related to the power extracted for a given rotation speed. Head is related to the power available to a constant flow rate [9]. This is in line with this study that the effect of the number of blades on the turbine vortex and the effect of the turbine depth were observed for different rotational speeds as shown in Fig. 5 and 6.

Fig. 5 shows the value for each variation in the number of blades increasing at the depth level used. Furthermore, the torque value obtained in this study is shown in Fig. 6. The results obtained is rotational speed, torque, and electric power. From the overall results, it is found that the highest value is owned by the turbine blade with the highest number of blades. This is because when the number of turbine blades is increased, it will affect the angle produced. Because the resulting angle will be smaller so that it will affect the cross-sectional area that will be exposed to the existing vortex flow.

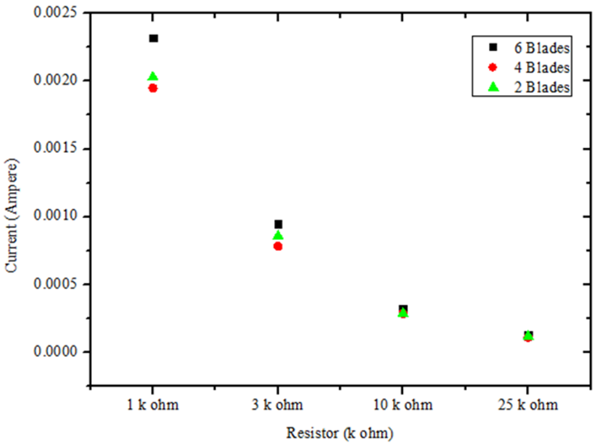

FIG. 7: The measured current as the function of resistance of the GWVPP with different number of blades.

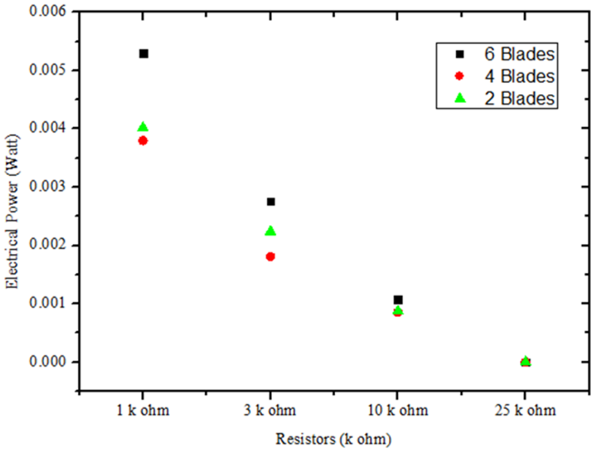

FIG. 8: The estimated power as the function of resistance of the GWVPP with different number of blades.

And for the influence of the weight of this turbine, it will be covered by the effect of the area imposed by the vortex flow.

Interestingly, the smallest value is not found in the small number of turbine blades. This is because when the number of blades is 4, it will make the resulting angle of 90 degrees. And with such an angle, it will result in the rotation of the turbine blade hampered, hence will reduce the rotation speed of the turbine. And for the number of 2 blades, it will form an angle of 180 degrees which does not have much impact in reducing the rotational speed of the turbine so that it will rotate normally but not too optimally. When the number of blades increased from two to six no significant difference was observed, but there was a slight reduction at higher rotations speed. The main reason for the increase in efficiency turbine with more number of blades is an increase torque. The current value against the resistance is shown in Fig. 7, and the electric power against the resistance is shown in Fig. 8.

Fig. 7 shows that the results of the highest current value is owned by the blade with a total number of 6 and the lowest value is owned by a blade with a total number of 4. Fig. 8 shows the increase in the yield of electrical power generated and is influenced by the number of turbine blades.

The values of rotational speed, torque, voltage, current, and power are related to each other. The highest rotational speed is achieved at 6 turbine blades, as well as that of the highest values for torque, voltage, current, and power. This is because they mutually influence each other in data collection. The overall conclusion of this study is to explain that the turbine with 6 blades has the highest value, and the turbine with 4 blades has the lowest value, both in terms of rotational speed, torque, voltage, current, and electric power.

Three main parameters are related: water level, velocity, and pressure contour. For turbines with different number of blades, its performance was observed to increase when the number of bar increased from two to six. When the knife number upgraded, the turbine exposes a large area to the vortex, extracting a relatively large amount of energy. Because of that, turbine torque increases at optimum rotation speed between 110 and 120 rpm. On the other hand, there is no significant change in performance noted when the number of blades is increased to four, although the effective area of the turbine increased significantly. This is because the four blade turbine will block the flow of water while avoiding the formation of an air core. In the presence of the vortex turbine, the air core splits and propagated behind the turbine blades, maintaining a low pressure area, while discharging the charge around the exhaust duct shop. Therefore, without an air core, a low pressure area is not maintained, and therefore, the pressure drop across the turbine blades is reduced.

IV. CONCLUSION

The number of blades affects the performance of the kinetic turbine. Electrical characteristics are highly dependent on the amount of torque and rotation. Water discharge is very influential on torque and rotation. At a discharge of 169.63 liters/minute, a conical basin with a square-shaped blade and variations in the number of blades, namely 2, 4, and 6 with the same turbine blade area of 0.01 m^2, the maximum data obtained for the mechanical characteristics of the 6-blade variation are 119.351 rpm, and the maximum value is 119.351 rpm with the torque of 0.762 Nm. The electrical characteristics are also found to be optimum when the number of blades is 6 with the maximum value of the 3.597 V voltage, the 0.00232 A current, and the the 0.005 W power. The results of the turbine rotation and torque measurements show that the number of blades sufficiently affects the mechanical characteristics of the turbine and the value of its electrical characteristics.

Acknowledgment

The authors would like to thank the Department of Physics, Faculty of Science and Data Analysis, Institut Teknologi Sepuluh Nopember (ITS) Surabaya for the support of research facilities so that this research can be carried out well.

---

[1] S. Pietersz, R. Soekono, R. Wahyudi, ”Pengaruh Jumlah Sudu terhadap Kinerja Turbin Kinetik Roda Tunggal,” *J. Rekayasa Mesin*, vol. 4, no. 3, pp. 220226, 2013.

[2] Warta Koperasi dan Usaha Mikro, Kecil dan Menengah (KUMKM), Warta KUMKM, vol. 5, no. 1, 2016.

[3] H. Of and S. O. F. Indonesia, ”Handbook of energy & economic statistics of Indonesia 2021,” 2021.

[4] N. F. Syafitri, ”Analisis Profil Sudu Turbin Mikro Hidro Vortex untuk mendapatkan efisiensi optimum, *Semin. Nas. Cendekiawan*, pp. 535541, 2018.

[5] O. B. Yaakob, Y. M. Ahmed, A. H. Elbatran, and H. M. Shabara, ”A review on micro hydro gravitational vortex power and turbine systems,” *J. Teknol. (Sciences Eng.)*, vol. 69, no. 7, pp. 17, 2014.

[6] A. Date and A. Akbarzadeh, ”Design and cost analysis of low head simple reaction hydro turbine for remote area power supply,” *Renew. Energy*, vol. 34, no. 2, pp. 409415, 2009.

[7] M. M. Rahman, J. H. Tan, M. T. Fadzlita, and A. R. Wan Khairul Muzammil, ”A Review on the Development of Gravitational Water Vortex Power Plant as Alternative Renewable Energy Resources,” *IOP Conf. Ser. Mater. Sci. Eng.*, vol. 217, no. 1, 2017.

[8] A. Sedai, B. K. Yadav, A. Khatiwada, and R. Dhakal, ”Performance analysis of Gravitational water vortex power plant using scale-down model,” *Current Research in Hydropower Technologies*, September, 2020.

[9] M.-S. Kim, D. S. Edirisinghe, H.-S. Yang, S. D. G. S. P. Gunawardane, and Y.-H. Lee, ”Effects of blade number and draft tube in gravitational water vortex power plant determined using computational fluid dynamics simulations,” *J. Adv. Mar. Eng. Technol.*, vol. 45, no. 5, pp. 252262, 2021.

The Use of Dirac Oscillator as Medium Substrate for Quantum Heat Engine

Heru Sukamto,[1] Bintoro Anang Subagyo,[1] and Agus Purwanto*[1]

[1]*Department of Physics, Institut Teknologi Sepuluh Nopember, Kampus ITS Sukolilo, Surabaya 60111, Indonesia*

Abstract: The research on Dirac oscillators has been increasing recently. In this paper, a quantum heat engine by means of a Dirac oscillator that interacts with the external magnetic field is proposed. Relativistic Landau energy levels are used to perform the iso-energetic cycle. The large magnetic field is set to obtain a perfect thermodynamic cycle. Some stable performances at a certain magnitude of magnetic field and expansion parameter range are obtained. When the value of efficiency is compared with the non-relativistic case, an opposite result occurs. Therefore, a quantum heat engine using a Dirac oscillator doesn't govern like a classical oscillator.

Keywords: Dirac Oscillator; Quantum Heat Engine; Iso-energetic Cycle

*Corresponding author: purwanto@physics.its.ac.id

Article history: Received 19 June 2022, Accepted 4 October 2022, Published October 2022.
http://dx.doi.org/10.12962/j24604682.v18i3.5282

I. INTRODUCTION

The quantum heat engine has been progressing lately, along with advances in nanotechnology. A wide range of medium substrates for quantum heat engines has been proposed, such as a one-dimensional potential well [1–5], a harmonic oscillator [6–8], etc. There have also been studied quantum heat engines with minimal length [9]. For one-dimensional potential well, the efficiency of non-relativistic and relativistic quantum heat engines have been compared. It was proved that the relativistic quantum heat engine in a potential well has a lower efficiency than the non-relativistic case [10].

A harmonic oscillator as a medium substrate without an external magnetic field has been carried out by utilizing the master equation [7]. Also, a quantum heat engine in non-relativistic cases has been studied using an external magnetic field which is analogous to the width of the potential well [11]. The thermodynamics processes are governed by a one-dimensional potential well quantum heat engine. The applied medium substrate is a single particle in a quantum dot semiconductor cylinder [12].

This paper discusses the quantum heat engine by means of a Dirac oscillator as a medium substrate. It is assumed that the spin on the Dirac oscillator will be ignored. The magnetic field is converted during the process so that the system undergoes a transition state. The magnetic field is set to obtain a perfect cycle. These models are expected to make a valuable contribution to quantum dot semiconductor applications.

II. DIRAC OSCILLATOR

A Dirac oscillator is the relativistic version of the quantum harmonic oscillator. There are several topics of Dirac oscillator in the case of (2+1) dimensions [13–15]. In this paper, the Dirac oscillator using an external magnetic field as a ref [13] is used. The Hamiltonian of the system is given by

$$H = c\boldsymbol{\alpha}\cdot\left(p - e\boldsymbol{A}/c - im\omega\beta\boldsymbol{r}\right) + \beta mc^2, \tag{1}$$

with **A** is the external magnetic field vector potential, e is electron charge that acts as the Dirac oscillator. In this model, the (2+1)-oscillator dimensions are considered, with the external magnetic field on the z-axis direction so that the vector potential is $\mathbf{A} = \left(-\frac{B}{2}y, \frac{B}{2}x, 0\right)$. Because of the two spatial dimensions, Pauli matrices become $\alpha_x = \sigma_x$, $\alpha_y = \sigma_y$, and $\beta = \sigma_z$. In order to get an analytic solution, mapping as ref. [13] is carried out, in order to obtain a modified Hamiltonian as follows

$$H = c\boldsymbol{\alpha}\cdot\left(\boldsymbol{p} - im\tilde{\omega}\beta\boldsymbol{r}\right) + \beta mc^2, \tag{2}$$

with $\tilde{\omega} = \omega - |e|B/2mc$. From the results of completion of the Dirac equation $H\Psi = E\Psi$, relativistic Landau energy levels are obtained as follows

$$E_n^{\pm} = \pm mc^2\sqrt{1 + \frac{4\hbar\tilde{\omega}}{mc^2}n},\ n = 1, 2, 3, .. \tag{3}$$

III. SINGLE PARTICLE QUANTUM HEAT ENGINE

According to Eq. (3), the energy levels of the system depend on the value of an external magnetic field. Then the energy of a single particle system is

$$E = \left\langle \hat{H} \right\rangle = \mathrm{Tr}\left(\hat{\rho}\hat{H}\right) = \sum_n p_n(B)E_n(B). \tag{4}$$

By differentiation, it shows

$$dE = \sum_n p_n(B)dE_n(B) + E_n(B)dp_n(B). \tag{5}$$

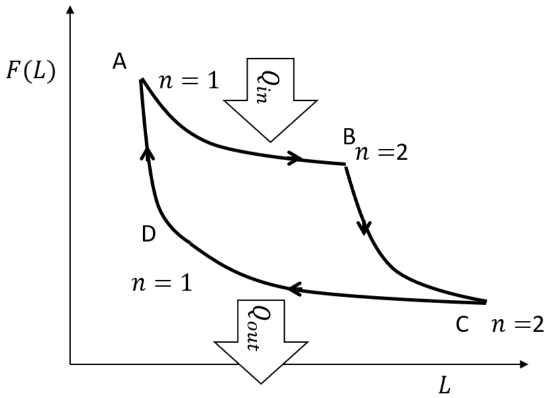

FIG. 1: Iso-energetic cycle. B represents an external magnetic field that is applied to the system, and M is the magnetization of the medium substrate

The energy equation above is analogous to the First Law of Thermodynamics.

$$dU = dQ - dW. \tag{6}$$

Because the probabilities of each state of the system is associated with entropy (von Neumann entropy).

$$S = -k_B \sum_n p_n(B) \ln p_n(B). \tag{7}$$

Then, the change in the total energy of the system is analogous to the change of internal energy in classical thermodynamics. On the right side, the first term of Eq. (5) is analogous to the work, and the second term is analogous to the heat exchange. The external magnetic field is related to the internal characteristics of the system, as well as the width of the potential well of the one-dimensional quantum heat engine. Thus, the change of the magnetic field does not provide an addition of heat to the system. During the iso-energetic process, the total energy is unchanged. An external magnetic field is set in a way that allows the system state changes from $n = 1$ to $n = 2$. During the process, all incoming heat is converted into work. Whereas during the adiabatic process, the magnetic field remains changing although there is no heat intake. The running of the magnetic field will change the energy level of each state as compensation for the work that has been done to the system.

IV. ISO-ENERGETIC PROCESSES

The iso-energetic cycle has two iso-energetic processes and two iso-entropic processes, as shown in Fig. 1. First, the iso-energetic AB is calculated in which the heat penetrating into the system changes completely into work. In this model, the initial state of the system is a ground state $n = 1$ with a constant magnetic field B_A. During the iso-energetic process, the magnetic field changes. At the end of the process, the system is fully in the state $n = 2$. During the process, the probability value and the total energy are changed as follows

$$p_1(B) + p_2(B) = 1, \tag{8}$$

$$p_1(B)E_1(B) + p_2(B)E_2(B) = E_1(B_A). \tag{9}$$

Based on the ref. [2], the value of the incoming heat is given by

$$Q_{AB} = \sum_n \int_{B_A}^{B_B} E_n(B) \frac{dp_n(B)}{dB} dB. \tag{10}$$

Using Eqs. (8) and (9), the heat value can be written as follows

$$Q_{AB} = \int_{B_A}^{B_B} \left[E_1(B) - E_2(B)\right] \frac{d}{dB} \left[\frac{E_1(B_A) - E_2(B)}{E_1(B) - E_2(B)}\right] dB. \tag{11}$$

Using Landau relativistic energy level Eq. (3), it shows

$$\begin{aligned} Q_{AB} = &-mc^2 \left[\tanh^{-1}\left(\frac{E_2(B_B)}{mc^2}\right) + \tanh^{-1}\left(\frac{E_1(B_B)}{mc^2}\right) \right. \\ &\left. - \tanh^{-1}\left(\frac{E_2(B_A)}{mc^2}\right) - \tanh^{-1}\left(\frac{E_1(B_A)}{mc^2}\right)\right]. \\ &- E_1(B_A) \ln\left[\frac{eB_B - 2m\omega c}{eB_A - 2m\omega c}\right] + \frac{1}{2} E_1(B_A) \ln\left[\frac{F(B_B)}{F(B_A)}\right] \end{aligned} \tag{12}$$

with

$$F(B) = 3ecB\hbar - m^2c^4 - 6mc^2\hbar\omega - E_1(B)E_2(B)$$

During process AB, the total energy of the system remains constant. Thus, the magnetic field at the end of the process AB satisfies

$$B_B = \frac{1}{2}B_A + \frac{m\omega c}{e}. \tag{13}$$

The value of the magnetic field is not the same as the non-relativistic case, as in ref. [11]. In this paper, the magnitude of the magnetic field at the end of the process depends on the mass m, charge e, and frequency ω. At the same time, the value ω will be determined by geometric scale $\ell_d = \sqrt{\hbar/m\omega}$. In the relativistic case, in order to obtain the fully final state $n = 2$, the magnitude of the magnetic field is also determined by these three parameters.

The following process is the iso-entropic process BC. During this process, there is no heat absorbed into the system. The work done by the system depends on changes in the internal energy. There is no state change, so the system is entirely on the state $n = 2$. Thus, during process BC, the work is given by

$$W_{BC} = E_2(B_C) - E_2(B_B). \tag{14}$$

By substituting Landau relativistic energy levels, it becomes

$$\begin{aligned} W_{BC} = &\, mc^2 \sqrt{1 + \frac{8\hbar}{mc^2}\left(\omega - \frac{eB_C}{2mc}\right)} \\ &- mc^2 \sqrt{1 + \frac{8\hbar}{mc^2}\left(\omega - \frac{eB_B}{2mc}\right)}. \end{aligned} \tag{15}$$

During the iso-entropy process, there is a change in the magnitude of the magnetic field from B_B to B_C. In the ref. [11], the iso-entropic process involves an expansion parameter. In order to make a good analogy, the geometric scale by an external magnetic field is defined as follows

$$\ell_B = \sqrt{\frac{\hbar}{m\omega_B}}, \tag{16}$$

with

$$\omega_B = \frac{eB}{m}. \tag{17}$$

So that the expansion parameter can be involved with

$$\frac{\ell_{B_C}}{\ell_{B_B}} = \alpha_1. \tag{18}$$

The expansion parameter α_1 is not written in a general form. The reason is the expansion parameter of the next iso-entropic process is not necessarily the same. Using Eqs. (16) and (17) show

$$B_C = \frac{1}{\alpha_1^2} B_B. \tag{19}$$

Then the cycle continues to the iso-energetic process CD. In this process, the state of the system changes from $n = 2$ state to $n = 1$ state again. Because the total energy remains constant, the process is fulfilled by

$$E_2(B_C) = E_1(B_D). \tag{20}$$

Thus obtained the relation

$$B_D = 2B_C - \frac{2m\omega c}{e}. \tag{21}$$

While the heat that comes out can be calculated by the integral as follows

$$Q_{CD} = \int_{B_C}^{B_D} [E_1(B) - E_2(B)] \frac{d}{dB}\left[\frac{E_2(B_C) - E_2(B)}{E_1(B) - E_2(B)}\right] dB, \tag{22}$$

resulting

$$\begin{aligned} Q_{CD} = -mc^2 \bigg[&\tanh^{-1}\left(\frac{E_1(B_D)}{mc^2}\right) + \tanh^{-1}\left(\frac{E_2(B_D)}{mc^2}\right) \\ &- \tanh^{-1}\left(\frac{E_1(B_C)}{mc^2}\right) - \tanh^{-1}\left(\frac{E_2(B_C)}{mc^2}\right)\bigg] \\ &- E_2(B_C)\ln\left[\frac{eB_D - 2m\omega c}{eB_D - 2m\omega c}\right] + \frac{1}{2}E_2(B_C)\ln\left[\frac{F(B_D)}{F(B_C)}\right]. \end{aligned} \tag{23}$$

And the later process is the iso-entropic process, in which the end of the process is returning to the initial state. The work during this process is

$$\begin{aligned} W_{DA} = &\, mc^2\sqrt{1 + \frac{4\hbar}{mc^2}\left(\omega - \frac{eB_A}{2mc}\right)} \\ &- mc^2\sqrt{1 + \frac{4\hbar}{mc^2}\left(\omega - \frac{eB_D}{2mc}\right)}, \end{aligned} \tag{24}$$

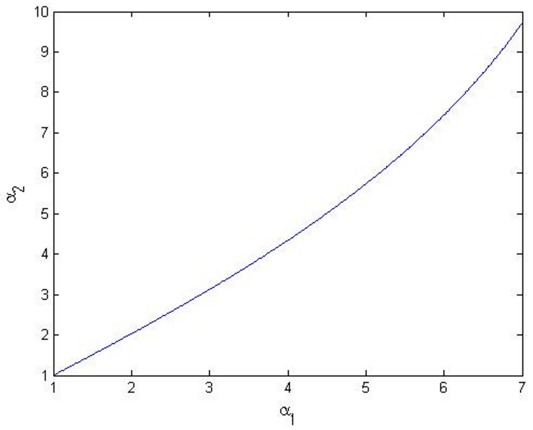

FIG. 2: Relation between α_1 and α_2.

with the geometry scale satisfies

$$\frac{\ell_{B_D}}{\ell_{B_A}} = \alpha_2. \tag{25}$$

the relationship of the initial and the final magnetic field is

$$B_D = \frac{1}{\alpha_2^2} B_A. \tag{26}$$

In order to obtain a reversible cycle, the magnitude of the magnetic field must satisfy the following cycle

$$B_A \xrightarrow[\frac{1}{2}B_A + \frac{m\omega c}{e}]{} B_B \xrightarrow[\frac{1}{\alpha_1^2}B_B]{} B_C \xrightarrow[2B_C - \frac{2m\omega c}{e}]{} B_D \xrightarrow[\alpha_2^2 B_D]{} B_A. \tag{27}$$

The first and second expansion parameter could be related as follows

$$\frac{\left(1 - \frac{\alpha_2^2}{\alpha_1^2}\right)}{2\left(\frac{\alpha_2^2}{\alpha_1^2} - \alpha_2^2\right)} = \frac{m\omega c}{eB_A}. \tag{28}$$

It can be illustrated by Fig. 2. According to Fig. 2, the value of the first expansion parameter α_1 is not necessarily the same as the second α_2. Then the efficiency of the machine can be obtained as

$$\eta = 1 - \frac{Q_{CD}}{Q_{AB}}, \tag{29}$$

substituting Eqs. (12), (13),(21), and (23) related as follows

$$\eta = 1 - \frac{\left[\tanh^{-1}\Theta(4a_C) - \tanh^{-1}\Theta(a_C)\right] - \frac{1}{2}\Theta(2a_C)\ln G(a_C)}{\left[\tanh^{-1}\Theta(a_A/2) - \tanh^{-1}\Theta(2a_A)\right] + \frac{1}{2}\Theta(a_A)\ln G(a_A)}, \tag{30}$$

we define

$$G(a) = \left[\frac{\frac{3}{4}a - \frac{1}{4} - \frac{1}{4}\Theta(a)\Theta(4a)}{\frac{3}{2}a - 1 - \Theta(a)\Theta(4a)}\right]$$

with $\Theta(a) = \sqrt{1 + a}$ and $a_A = \frac{4\hbar}{mc^2}\left(\omega - \frac{eB_A}{2m}\right)$, $a_C = \frac{4\hbar}{mc^2}\left(\omega - \frac{eB_C}{2m}\right)$. Variable a_A and a_C are related by $a_C =$

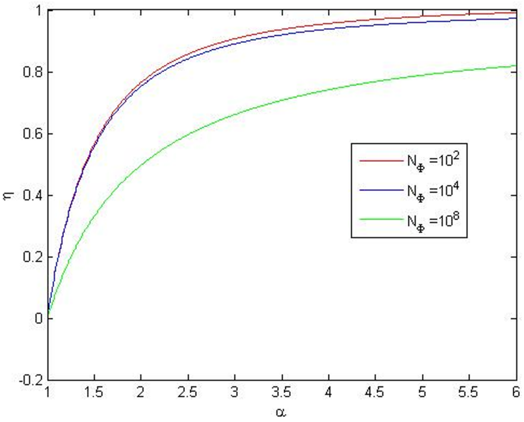

FIG. 3: Relation between expansion parameter with the efficiency by initial magnetic field with various B_A. We choose $\ell_d = 10^{-7}\ m$.

$\frac{1}{2\alpha_1^2}a_A + \frac{4\hbar}{mc^2}\omega\left(1 - \frac{1}{\alpha_A^2}\right)$. We define N_Φ as a quantity that expressed the value of initial magnetic field B_A as $B_A = \frac{2m\omega}{e}N_\Phi$. Due to relativistic property, not all values of N_Φ producing all cyclic processes. It can be said initial value of the magnetic field is large enough and has a minor change during the iso-energetic cycle. From Fig. 3, it appears that the greater the magnetic field, the smaller the engine efficiency. That differs from the ref [11], which provides the opposite conclusion.

V. DISCUSSION AND CONCLUSION

A Quantum heat engine with the Dirac oscillator as the substrate medium produces engine efficiency values through an isoenergetic cycle. In the non-relativistic case, the efficiency is proportional to the initial value of the magnetic field. In a relativistic case, this happens inversely. The larger the initial magnetic field, the smaller the efficiency value. Moreover, what should be noted is that not all initial magnetic field values produce cyclic cycles in a quantum heat engine using the Dirac oscillator as the substrate medium. The expansion parameter's value also affects the engine's efficiency, as in the non-relativistic case.

VI. ACKNOWLEDGMENT

The authors thank LPPM ITS for supporting this research through the departmental funding research program number 1753/PKS/ITS/2022.

---

[1] C. M. Bender, D. C. Brody, and B. K. Meister, “Quantum mechanical carnot engine,” *Journal of Physics A: Mathematical and General*, vol. 33, no. 24, p. 4427, 2000.
[2] H.-T. Quan, Y.-x. Liu, C.-P. Sun, and F. Nori, “Quantum thermodynamic cycles and quantum heat engines,” *Physical Review E*, vol. 76, no. 3, p. 031105, 2007.
[3] C. M. Bender, D. C. Brody, and B. K. Meister, “Entropy and temperature of a quantum carnot engine,” *Proceedings of the Royal Society of London. Series A: Mathematical, Physical and Engineering Sciences*, vol. 458, no. 2022, pp. 1519–1526, 2002.
[4] J. Wang and J. He, “Optimization on a three-level heat engine working with two noninteracting fermions in a one-dimensional box trap,” *Journal of Applied Physics*, vol. 111, no. 4, p. 043505, 2012.
[5] E. Latifah and A. Purwanto, “Multiple-state quantum carnot engine,” *Journal of Modern Physics*, vol. 2011, 2011.
[6] B. Lin and J. Chen, “Performance analysis of an irreversible quantum heat engine working with harmonic oscillators,” *Physical Review E*, vol. 67, no. 4, p. 046105, 2003.
[7] Y. Rezek and R. Kosloff, “Irreversible performance of a quantum harmonic heat engine,” *New Journal of Physics*, vol. 8, no. 5, p. 83, 2006.
[8] J. Arnaud, L. Chusseau, and F. Philippe, “Carnot cycle for an oscillator,” *European journal of physics*, vol. 23, no. 5, p. 489, 2002.
[9] A. Purwanto, H. Sukamto, B. Subagyo, *et al.*, “Quantum carnot heat engine efficiency with minimal length,” *Journal of Modern Physics*, vol. 6, no. 15, p. 2297, 2015.
[10] E. Munoz and F. J. Pena, “Quantum heat engine in the relativistic limit: The case of a dirac particle,” *Physical Review E*, vol. 86, no. 6, p. 061108, 2012.
[11] E. Munoz and F. J. Pena, “Magnetically driven quantum heat engine,” *Physical Review E*, vol. 89, no. 5, p. 052107, 2014.
[12] D. Englund, D. Fattal, E. Waks, G. Solomon, B. Zhang, T. Nakaoka, Y. Arakawa, Y. Yamamoto, and J. Vučković, “Controlling the spontaneous emission rate of single quantum dots in a two-dimensional photonic crystal,” *Physical review letters*, vol. 95, no. 1, p. 013904, 2005.
[13] B. Mandal and S. Verma, “Phys. lett. a,” 2010.
[14] B. P. Mandal and S. K. Rai, “Noncommutative dirac oscillator in an external magnetic field,” *Physics Letters A*, vol. 376, no. 36, pp. 2467–2470, 2012.
[15] D. Nath and P. Roy, “Dirac oscillator in perpendicular magnetic and transverse electric fields,” *Annals of Physics*, vol. 351, pp. 13–21, 2014.

JFA (Jurnal Fisika dan Aplikasinya)
Information for Authors

JFA (Jurnal Fisika dan Aplikasinya) only publishes original research results, has never been published elsewhere and is not in the process of being considered for publication elsewhere, in any language.

MANUSCRIPTS

The manuscripts should be written with double spaces on A4 paper with margins: left $\sim$ 3 cm, top $\sim$ 2.5 cm, right $\sim$ 2.5 cm, under $\sim$ 2.5 cm, with one column layout (two-column layout will be done by the editor team), and it is strongly recommended to use LaTeX with REVTeX$\sim$4-*style*. However, papers are written using a *word processor* like MS-word, we still accept it.

Language: The manuscripts are written in Indonesian or English, and starting in 2021 all manuscripts are written in English.
Author's name: The author's name is written in full (without title/designation) together with affiliation and full address. The corresponding author must write their email address.
Abstract: The abstract is written with no more than 200 words, and contains important aspects and the main results of the research. Abstract written in Indonesian and English, and starting in 2021 only English.
Keywords. Each manuscript must be accompanied by keywords, a maximum of 4 (four) keywords and each keyword is separated by a semicolon (;). Keywords are written in English.

FIGURE AND TABLE

Each figure and table must be given a clear description and be made on a separate paper (not attached to the manuscript). Figures and tables must be numbered in the order they appear. Footnotes for the contents of the table must be written directly below the table. If quoting images, tables or photos from other publishers, the author must specify the source.

EQUATION

Each equation must be numbered in the order they appear.

LIST OF REFERENCES

The list of references is placed at the end of the manuscript, numbered in Arabic numerals in harmony with the order in which the text is referenced, for example, "According to a recent experimental result [1] ...". There is a change in the style of writing a reference list starting in the 2018 edition (volume 14) using the IEEE style, with the following pattern:

[1] S. Li and W. Sun, "A comparative study on aggregation/sedimentation of TiO_2 nanoparticles in mono- and binary systems of fulvic acids and Fe(III)", J. Hazard. Mater., vol. 197, pp. 70-79, Dec. 2011.

[2] C.G. Granqvist, "Thin films and nanostructured coatings for eco-efficient buildings", in "Nanotechnology in Eco-Efficient Construction", F. Pacheco-Torgal, M. V. Diamanti, A. Nazari, and C.-G. Granqvist, Eds. Woodhead Publishing, 2013, p. 161-187a.

[3] M. Dressel and G. Grner, "Electrodynamics of Solids: Optical Properties of Electrons in Matter", 1 edition, Cambridge University Press, Cambridge, New York, 2002.

[4] G. Yudoyono, *et al.*, "Effect of calcination temperature on the photocatalytic activity of TiO_2 powders prepared by co-precipitation of $TiCl_3$", in AIP Conference Proceedings 1725, Semarang, Indonesia, 2016, vol. 1725, p. 020099.

[5] H. Santoso, "Fabrikasi dan Karakterisasi Dye-Sensitized Solar Cells (DSSC) menggunakan Dye sensitizer Sintetis N-749", Thesis, Institut Teknologi Sepuluh Nopember, Surabaya, Indonesia, 2015.

Unpublished data or only the result of personal communication, may not be included in the reference list.

In each manuscript contains the following section (except special topics that cannot follow this format can be in the format commonly used in the topic):

1. **Abstract** (contains a summary of background, methods, results, and conclusions)
2. **Introduction** (contains "the state of the art" of the problem written in the manuscript)
3. **Methodology** (contains a process or scientific way to get data written in a concise and concise)
4. **Results and discussion** (contains the results obtained and discussion of aspects of theoretical studies, aspects of empirical studies, and aspects of the implications of results)
5. **Conclusions** (outline the contents of the manuscript outline)

You can add an acknowledgment that should only be given to those who directly contribute to articles written, such as financial aid providers, experts involved through correspondence.

REVISION

The manuscripts that are submitted will be conducted an initial assessment by a team of editors related to the suitability of journal goals. All texts sent will be checked for potential plagiarism using the ”iThenticate” software. Then the article will be sent to the reviewer and will be selected by the single-blind method. JFA reviewers are experts in physics and its applications. They have experience in leading journal management and have published papers at national and international levels. In each text, reviewers will assess the substance of the technical aspects of the article. The assessment criteria include originality, the correctness of content, clarity of description, and suitability of the target journal with the review process. After that, the article will be returned to the author for revision. The author should revise according to comments/suggestions from reviewers and editors. However, the author has the right to rebut the comments/suggestions of the reviewer and editor.

EDITORIAL ADDRESS

The manuscripts should be sent to:

JFA (Jurnal Fisika dan Aplikasinya)
Departemen Fisika, Fakultas Sains dan Analitika Data,
Kampus ITS, Keputih
Sukolilo Surabaya 60111
Telp.:(031)5943351; Fax.: (031)5943351
E-mail: jfa@physics.its.ac.id
jfa.fisika.its@gmail.com
Web site: http://iptek.its.ac.id/index.php/jfa/index

Correspondence regarding the manuscript should be sent to the above address, mentioning the manuscript ID, and the author’s name.